NASA Contractor Report 186016

Thrust Vectoring for Lateral-Directional Stability

Lee R. Peron and Thomas Carpenter

NASA

National Aeronautics and
Space Administration

NASA Contractor Report 186016

Thrust Vectoring for Lateral-Directional Stability

Lee R. Peron and Thomas Carpenter
California Polytechnic State University, San Luis Obispo, California

NASA

National Aeronautics and
Space Administration

Dryden Flight Research Facility
Edwards, California 93523-0273

This Page Intentionally Left Blank

CONTENTS

FIGURES

ABSTRACT

This investigation was conducted to determine the advantages and disadvantages of using thrust vectoring for lateral-directional control and the effects of reducing the tail size of a single-engine aircraft. The aerodynamic characteristics of the F-16 aircraft were generated by using the Aerodynamic Preliminary Analysis System II panel code. The resulting lateral-directional linear perturbation analysis of a modified F-16 aircraft with various tail sizes and yaw vectoring was performed at several speeds and altitudes to determine the stability and control trends for the aircraft compared to these trends for a baseline aircraft. A study of the paddle-type turning vane thrust vectoring control system as used on the National Aeronautics and Space Administration F/A-18 high alpha research vehicle is also presented.

INTRODUCTION

Increasing interest in the use of thrust vectoring control systems to enhance or replace aerodynamic controls for future fighter aircraft exists. Pitch vectoring nozzles have the potential to increase turn performance, reduce drag, and increase short field flight operations through careful nozzle integration and optimum vectoring. The benefits of yaw vectoring include directional control power at low speeds, at high angles of attack, and during spins and stalls, where the traditional control surface effectiveness is substantially reduced. Reduction of vertical tail size by using thrust vectoring control power also promises to benefit aircraft observability and to reduce drag and weight substantially; however, the addition of the thrust vectoring control system may eliminate some of these benefits.

Now, several aircraft incorporate thrust vectoring in the control systems. The F-15 short takeoff and landing maneuver technology demonstrator and the proposed advanced tactical fighter have pitch vectoring nozzles, while the X-31 aircraft and F/A-18 high alpha research vehicle incorporate pitch and yaw vectoring through use of postexit vanes. Pratt & Whitney Co. (West Palm Beach, Florida) is developing a lightweight, highly efficient, three-dimensional nozzle to replace the current nozzles on America's F-14, F-15, and F-16 fighter aircraft.

Purpose

The fighter aircraft of the future will require use of thrust vectoring controls to attain the maximum controllability during maneuvers and optimum performance. Thrust-vectoring controls will work in conjunction with traditional aerodynamic control surfaces to enhance the longitudinal- and lateral-directional flying characteristics of the aircraft. This study describes the significant effects of thrust vectoring control systems and reduction of vertical tail size on lateral-directional stability and control of a single-engine fighter aircraft.

Aircraft Description

For this study, the F-16 single-seat fighter aircraft with the F-100 engine model derivative and four postexit thrust vectoring control vanes was employed. The General Dynamics (Fort Worth, Texas) F-16 aircraft is a small, single-engine, single-seat, multirole, tactical fighter known for its high performance and agility (fig. 1). The wing of the F-16 aircraft has a moderate sweep and automatic leading-edge

flaps and flaperons. The flaperons combine the functions of automatic trailing-edge flaps and ailerons and provide pitch and roll control. The all-moving horizontal tail has a small amount of anhedral and provides both pitch and roll control through symmetric and differential deflections. The vertical tail and two ventral fins provide directional stability, while rudder deflections on the vertical tail provide directional control (refs. 1 and 2).

The F-16 aircraft incorporates an analog flight control system with a force-sensing sidestick controller and associated feedback loops, gain schedules and limiters for angle of attack, g loading, roll and yaw rates, and rudder pedal force. The current roll and yaw rate limiters automatically engage at high angles of attack and are coupled to the roll and yaw rates and the angle of attack (ref. 3).

The engine of the F-16 aircraft used in this study is a modified version of the currently deployed F-100 engine known as the F-100 engine model derivative and was used in the F-15 highly integrated digital electronic control aircraft at the NASA Dryden Flight Research Facility. The F-100 engine model derivative (company designation PW 1128/Pratt & Whitney, West Palm Beach, Florida) is a low bypass, twin-spool afterburning, turbofan engine (ref. 4). The primary nozzle throat area is controlled by digital electronic engine control. Aircraft trends indicate that the thrust vectoring and reversing aircraft will employ digital electronic control systems such as highly integrated digital electronic control and full authority digital engine control and will allow an improved engine performance, a larger flight envelope, a faster stall-free engine acceleration, a lower specific fuel consumption, and a safer operation as it reduces the pilot's workload during takeoffs and landings (ref. 5).

For this report, an engine simulation program that predicts the engine performance through component characteristics was used. The F-100 specification model is a steady-state, aerodynamic, mathematical model of the F-100 engine model derivative turbofan engine used to obtain the predicted net thrust, gross thrust, and nozzle pressure ratios at specified altitudes and Mach numbers (ref. 4).

A thorough analysis of the thrust vectoring control system being installed on the F/A-18 high alpha research vehicle at NASA Dryden was used to build the thrust vectoring control system model used in this study. The three nickel alloy Inconel (International Nickel Company, Huntington, West Virginia) postexit vanes that were cold-jet tested at the NASA Langley Research Center (Langley) for the F/A-18 high alpha research vehicle were used to model a four-vane system proposed for the F-16 aircraft.

Project Scope

The lateral-directional linear perturbation analysis of the F-16 aircraft with various tail sizes was performed at a wide range of altitudes and speeds to determine the stability and control envelope. The aerodynamic data were obtained by constructing several models of the F-16 aircraft using the aerodynamic preliminary analysis system panel code. Postexit vane efficiency and effectiveness were obtained by analyzing the thrust vectoring control system cold-jet tests of the F/A-18 high alpha research vehicle at NASA Langley. Next, a linear perturbation analysis program called Stability 1 was constructed to obtain the stability and control characteristics. This program incorporated the cold-jet efficiency and effectiveness correlations, the Aerodynamic Preliminary Analysis System II aerodynamic coefficients completed for this study, and the results of the F-100 engine specification deck and NASA Langley's wind-tunnel tests of thrust induced effects on the high alpha research vehicle.

2

Organization

This report is comprised of sections dealing with the advantages of thrust vectoring control systems, a discussion of thrust vectoring control systems, the aerodynamics of the aircraft, the stability analysis results, and the conclusions and recommendations.

NOMENCLATURE

Abbreviations

APAS	Aerodynamic Preliminary Analysis System II
ATF	advanced tactical fighter
DEEC	digital electronic engine control
EMD	engine model derivative
FADEC	full authority electronic control
HARV	high alpha research vehicle
HIDEC	highly integrated electronic control
LCSP	lateral coefficient spin parameter
LEF	leading-edge flap
NASA	National Aeronautics and Space Administration
NPR	nozzle pressure ratio
PEV	postexit vanes
PSM	poststall maneuver
SPEC	F-100 engine specification deck
STAB1	Stability-1 computer program
STOL	short takeoff and landing
TOGW	takeoff gross weight
TVCS	thrust vectoring control system

List of Symbols

A	constant
AR	aspect ratio
ARC	radial vane size
B	constant
b	wing span
C_D	drag coefficient
$C_{D_{\text{skin friction}}}$	skin friction drag coefficient
$C_{L_\alpha} = \frac{\partial C_\ell}{\partial \alpha}$	lift slope curve, deg
$C_{L_{\delta_{\text{LEF}}}} = \frac{\partial C_\ell}{\partial \delta_{\text{LEF}}}$	variation of lift coefficient with leading-edge flap deflection angle, deg
$C_{\ell_p} = \frac{\partial C_\ell}{\partial p}$	variation of rolling moment coefficient with roll rate, rad

$C_{\ell_r} = \frac{\partial C_\ell}{\partial r}$ variation of rolling moment coefficient with yaw rate, rad

$C_{\ell_\beta} = \frac{\partial C_\ell}{\partial \beta}$ variation of rolling moment coefficient with sideslip angle, deg

$C_{\ell_\delta} = \frac{\partial C_\ell}{\partial \delta}$ variation of rolling moment coefficient with control angle, deg or rad

$C_{\ell_{\delta r}}$ variation of rolling moment coefficient with rudder deflection, deg

$C_{n_p} = \frac{\partial C_n}{\partial p}$ variation of yawing moment coefficient with roll rate, rad

$C_{n_r} = \frac{\partial C_n}{\partial r}$ variation of yawing moment coefficient with yaw rate, rad

$C_{n_\beta} = \frac{\partial C_n}{\partial \beta}$ variation of yawing moment coefficient with sideslip angle, deg

$C_{n_\delta} = \frac{\partial C_n}{\partial \delta}$ variation of yawing moment coefficient with control angle, deg or rad

$C_{n_{\delta r}}$ variation of yawing moment coefficient with rudder deflection, deg

$C_{y_p} = \frac{\partial C_y}{\partial p}$ variation of side force coefficient with roll rate, rad

$C_{y_r} = \frac{\partial C_y}{\partial r}$ variation of side force coefficient with yaw rate, rad

$C_{y_\beta} = \frac{\partial C_y}{\partial \beta}$ variation of side force coefficient with sideslip angle, deg

$C_{y_\delta} = \frac{\partial C_y}{\partial \delta}$ variation of side force coefficient with control angle, deg or rad

$C_{y_{\delta r}}$ variation of side force coefficient with rudder deflection, deg

c chord

c.g.   center of gravity

D drag, lb

F force, lb

G gain

g acceleration because of gravity, ft/sec^2

h height

I moment/product of inertia, slug/ft^2

K transfer function constant

k constant

L rolling moment, ft·lb

$L_p = \frac{C_{\ell_p} \bar{q} S b^2}{2 U_0 I_{xx}}$ dimensional variation of rolling moment with roll rate, sec

$L_r = \frac{C_{\ell_r} \bar{q} S b^2}{2 U_0 I_{xx}}$ dimensional variation of rolling moment with yaw rate, sec

$L_\beta = \frac{C_{\ell_\beta} \bar{q} S b}{I_{xx}}$ dimensional variation of rolling moment with sideslip angle, sec^2

$L_\delta = \frac{C_{\ell_\delta} \bar{q} S b}{I_{xx}}$ dimensional variation of rolling moment with control angle, sec^2

M Mach number/pitching moment, rad/sec

m mass, slugs

N yawing moment, ft·lb

$N_p = \frac{C_{n_p} \bar{q} S b^2}{2 U_0 I_{zz}}$ dimensional variation of yawing moment with roll rate, sec

$$N_r = \frac{C_{n_r}\bar{q}Sb^2}{2U_0 I_{zz}}$$ dimensional variation of yawing moment with yaw rate, sec

$$N_\beta = \frac{C_{n_\beta}\bar{q}Sb}{I_{zz}}$$ dimensional variation of yawing moment with sideslip angle, sec^2

$$N_\delta = \frac{C_{n_\delta}\bar{q}Sb}{I_{zz}}$$ dimensional variation of yawing moment with control angle, sec^2

n	g level
P	roll rate, rad/sec
p	roll rate, rad/sec
$\hat{p}$	transfer function pole
Q	pitch rate, rad/sec
q	pitch rate, rad/sec
$\bar{q}$	dynamic pressure, lb/ft^2
R	yaw rate, rad/sec
r	small perturbation yaw rate, rad/sec
S	wing area, ft^2
s	Laplace variable
T	thrust, lb
t	time, sec
U	aircraft forward velocity, ft/sec
u	small perturbation velocity, ft/sec
$\dot{u}$	small perturbation acceleration, ft/sec^2
V	aircraft side velocity, ft/sec
v	small perturbation velocity, ft/sec
W	vertical velocity, ft/sec
W_t	weight, lb

$$Y_p = \frac{C_{y_p}\bar{q}Sb}{2U_0 m}$$ dimensional variation of side force with roll rate, ft/sec

$$Y_r = \frac{C_{y_r}\bar{q}Sb}{2U_0 m}$$ dimensional variation of side force with yaw rate, ft/sec

$$Y_\beta = \frac{C_{y_\beta}\bar{q}S}{m}$$ dimensional variation of side force with sideslip angle, ft/sec^2

$$Y_\delta = \frac{C_{y_\delta}\bar{q}Sb}{m}$$ dimensional variation of side force with control angle, ft/sec^2

$\hat{z}$	transfer function zero

Greek Symbols

α	angle of attack, deg
β	sideslip angle, rad or sec
Δ	characteristic equation
δ	control angle, rad or deg
γ	exponent for weight equation
ζ	damping ratio
θ	pitch angle, deg
Λ	sweep angle, deg

λ	taper ratio
$\bar{\rho}$	density, slug/ft^3
ϕ	roll angle, rad
Ψ	heading angle, rad
Ω	radial vane position angle, deg
ω	frequency, rad/sec

Subscripts

a	aileron
base	base drag
dynamic	dynamic spin parameter
ht	horizontal tail
r	rudder
$s.l.$	sea level
to	takeoff
tot	total
tv	thrust vectoring
TVCS	thrust vectoring control system
vt	vertical tail
vector	thrust vector
x	x-axis
y	y-axis
z	z-axis
0	body axis
1	inertial constant
100%	tail size, percent

ADVANTAGES OF THRUST VECTORING CONTROL SYSTEMS

The future air warfare arena will be quite demanding and will require improvements in agility, control, performance, short takeoff and landing (STOL) capabilities, and stealth. The use of thrust vectoring is being considered as a way to accommodate these demands.

Agility

Aircraft agility can be defined as the aircraft's maneuver and control capabilities, that is, the ability to maneuver and point quickly, to obtain first-shot advantage over an opponent, to sustain high-turn rates, accelerations, and decelerations, and to perform offensive and defensive maneuvers at will (refs. 6 and 7). Agility is currently measured by pitch rate, load factor, turn performance, roll rate, level yaw rates, and acceleration and deceleration (ref. 8).

History shows that aircraft designed during times of war tend to have greater agility than those designed during times of peace (ref. 9). The F-16 aircraft was designed for high maneuverability;

6

however, its wing loading has increased substantially as avionics and weapons systems have been added over the years. To compensate for the loss of maneuverability, a modified F-16 aircraft, the Agile Falcon, with an increase in wing area and the addition of thrust vectoring has been proposed. Maneuverability is important; however, improvements in maneuverability must be accompanied by increased controllability or overall agility will suffer. During the Korean conflict, the MiG 15 aircraft had greater maneuverability than its adversary, the F-86 aircraft; however, the F-86 aircraft had greater controllability and was able to rack up an impressive ratio of air victories (ref. 8).

Controllability is the quickness of ease to change the flightpath of the aircraft from moments and forces caused by the control surfaces. In addition, controllability gives the option of stepping out of the limits of optimum efficiency or to an arena of stability not considered normal. Unfortunately, current flight controls of the F-16 aircraft try to prohibit unstable high angle-of-attack maneuvers through use of pitch, roll, and yaw rate limiters. The goal of increasing controllability is to increase the envelope of positive control for the pilot, especially at high angles of attack or sideslip. A solution for increased controllability demands is for a thrust vectoring control system (TVCS) to provide the required forces and moments (ref. 6).

The F-15 short takeoff and landing (STOL) maneuver technology demonstrator (MTD), which incorporates a two-dimensional pitch TVCS, is designed to have increased turn performance, 33 percent improvement in pitch rate and 53 percent improvement in roll rate because of the TVCS (ref. 10). As pitch and roll are enhanced, yaw rate promises to be substantially increased because of yaw vectoring, especially at high angles of attack where roll and yaw rates are seriously degraded due to the control surfaces being blanked out by the disturbed flow of the aircraft wing.

Poststall Maneuvering

There has been a recent trend toward the exploration of poststall maneuvers (PSM) through studies and flight aircraft. The Russian demonstration at the 1989 Paris airshow of a production Su-27 performing a Pugachev's Cobra, where the aircraft obtains an angle of attack greater than 90° without loss of control, has reemphasized the importance of exploring this regime (ref. 11). Currently, NASA Dryden Flight Research Facility (Dryden) is flight testing the F/A-18 high alpha research vehicle (HARV), which has achieved studies in angles of attack of up to 55°, and is dedicating flights of the X-29 aircraft to the study of forward-swept wings at high angle of attack (ref. 12).

Poststall maneuvering increases close-combat effectiveness by allowing the advantage of quicker entry into and longer maintenance of firing position, more first-shot opportunities, and fewer counter hits. Poststall maneuvering studies indicate that it is easier and quicker to switch targets, deploy missiles, and dictate tactics throughout the entire speed regime. These advantages lead to an exchange ratio of 2:1 in dual-combat studies against opponents of equal conventional aircraft (ref. 7).

The Herbst maneuver is traditionally associated with a short excursion into the poststall regime and then a return to normal flight. As a combat technique, the Herbst maneuver is characterized by its high angle of attack; its short duration, an average of 5 sec; and its use in 10 percent of engagement time, lower overall g levels, and lower overall speeds during air-combat simulations (ref. 7). Longer poststall maneuvers include a helicopter maneuver that allows pilots to track the target by yawing instead of using

7

a coordinated turn and a fully controlled tail slide maneuver that allows pilots to track an opponent that is attacking from above. Poststall maneuvers traditionally have high pitch rates and include simultaneous rotations in roll and yaw (ref. 13).

H. Ashley found that in real-time simulation studies that high-angle-of-attack requirements are highly oscillatory and unsteady and require large forces and moments over a wide range of attitudes (ref. 14). He suggests that $\pm 10°$ of total jet deflection of thrust are needed to supply control because of the inadequacy of the aerocontrols.

For a pilot in an offensive position, pitch and yaw vectoring can be a powerful maneuver depending on the type of opponent, the opponent's flight regime, and the ability to optimize maneuvers. If both aircraft are not in a low-speed flight regime, entering a poststall maneuver, where thrust vectoring would be employed while the opponent maintained a higher energy state, would be a great disadvantage. Furthermore, if both aircraft are in low-speed flight, the pilot must perform an optimum maneuver to gain the maximum advantage. Pitch and yaw vectoring tends to be less effective at the lower altitudes because the advantages of turn rate are negligible. The advantages in turn rate and agility zone increase as altitude increases. It is advisable to incorporate yaw vectoring into the controls and to have the option of turning on or off the pitch vectoring at the pilot's discretion. Simulation studies showed that pilots require larger positive acceleration because of gravity (g) loading and upward pitch vectoring than downward pitch vectoring. Because poststall maneuvers and short takeoffs require large vector-up deflections, while the downward vector requirements for optimum performance are usually less than $10°$, tilt the nozzle to increase the upper limits of the vectoring envelope.

Stealth

The one area in which great benefits can be achieved through the use of thrust vectoring is that of stealth. Because radar cross-section is a measure of the observability of the aircraft and is an logarithmic function of the profile area presented by the aircraft, small reductions in this area realize great benefits. From a side view of the aircraft, the fuselage, cockpit, and vertical stabilizer are the main contributors of observability (ref. 15). The current stealth modifications to the F-16 aircraft include radar absorbing materials in the intake and a reflective gold-covered canopy. Because the fuselage size is relatively constant, it can be concluded that the reduction of the vertical stabilizer has the largest room for improvement (ref. 16). The addition of a TVCS may nominally increase the observability of the aircraft, but a large reflective vertical tail is harder to mask than a faired TVCS. Quantitative improvements in radar observability are very difficult to predict and require thorough testing. The amount that the tail size can be reduced is largely a consideration of the dynamic stability and control of the aircraft.

Thrust Vectoring Concepts

In the past, most TVCSs have been developed for pitch vectoring concepts such as the F-15 S/MTD in a trend toward developing short field capability technology and performance optimization. In recent years, the interest in PSM has increased the investigations of pitch and yaw vectoring concepts. Similar in application, pure yaw vectoring concepts are less beneficial in overall aircraft performance than pure pitch vectoring two-dimensional nozzles.

There are two types of nozzle classifications: the nonaxisymetric nozzle and the conventional axisymmetric nozzle. The nonaxisymmetric nozzle concepts typically employ sidewall flaps or rectangular ports to affect the direction, while the typical axisymmetric nozzles mechanically turn all or part of the nozzle or employ postexit vanes. With nonaxisymmetric nozzles, rounded or rectangular nozzles are simpler to implement vectoring and have fewer moving parts than an axisymmetric nozzle with variable throat control. At low Mach numbers, twin-engine aircraft with nonaxisymmetric nozzles have lower drags, but as the Mach number increases to the transonic region, the axisymmetric nozzles exhibit lower overall drags. In addition, nonaxisymmetric nozzles may be more sensitive to adverse tail effects than axisymmetic nozzles at transonic and supersonic Mach numbers where these effects are significant (ref. 17).

The TVCS have several disadvantages, the primary of which is the reduction of thrust performance and the lost nozzle efficiencies. Losses occur in nozzles because of skin friction, internal flow separation, exhaust flow divergence, under- and overexpansion, and temperature and thrust distortions. Turning the gross thrust from axial direction also causes losses in nozzles. For postexit vanes, additional skin friction and pressure losses are caused by the thrust vectoring hardware (ref. 18).

Two-dimensional, rectangular, nonaxisymmetric nozzles integrate well with tapering nearly rectangular aftbody fuselage contours, thereby offering a potential reduction in the nozzle airframe drag during cruise (ref. 18). For twin-engine aircraft, this configuration would have favorable effects with nozzle airframe-induced drag. With careful attention, nozzle boat tailing can be eliminated in the immediate vicinity of the nozzle interfairings, tail-support boom structure, and empennage surfaces, and, therefore, in minimizing nozzle aft end-flow separations. Through the positive effects of optimum vectoring, drag reductions of up to 13 percent have been obtained (ref. 19). Drag reductions from axisymmetric and nonaxisymmetric nozzles can be made by careful attention to the wing-body geometry and its interaction with the flowfield. Success depends on the local contouring and the rate of area change of aftbody nozzle area. The drag reductions are the most significant by use of the thrust-induced, supercirculation effects for enhancing effects at maneuver conditions. The very dramatic changes between the jet-on and jet-off conditions, even when unvectored, display complex characteristics that will require greater levels of understanding than conventionally employed in nozzle design and airframe integration (ref. 20).

The structural efficiency of nonaxisymmetric nozzles is less than that of axisymmetric nozzles. Further weight gains can be attributed to the fact that the engine case structure must be strengthened to withstand the vectoring. Takeoff gross weight penalties from 5 to 7 percent occur because of the structural effects and cooling system weights (ref. 18). In one study, the weight of a prototype three-dimensional thrust vectoring nozzle on an RB199 engine was 254 lb (ref. 13). For the postexit vanes of the F/A-18 HARV, the total weight gain was 1200 lb for the TVCS for a 3.33 percent increase in takeoff gross weight (TOGW). In addition, there was an 800 lb increase or 2.22 percent greater TOGW for the counterbalance weight to maintain aircraft center of gravity (c.g.) position. For the postexit vanes (PEV), the TVCS comes to 200 lb/vane.

At this time, Pratt & Whitney is developing an axisymmetric balanced beam pitch and yaw vectoring nozzle for installation on fighter aircraft with very little weight increase. This new design incorporates many standard, nonvectoring, engine nozzle components and can have ratios of thrust deflection over nozzle deflection greater than unity. When this system is operational, the PEV thrust-vectoring system

will be obsolete. For this study, postexit vanes are used because of the availability of data and to demonstrate the maximum effects of implementing a thrust-vectoring system.

THRUST VECTORING CONTROL SYSTEM

The choice of an axisymmetric nozzle with paddle-type postexit vanes was based on modifying the F-16 aircraft using the current technology of the F/A-18 HARV and X-31 aircraft programs. These projects chose to implement PEV because installation is relatively simple, and it is time and cost effective in demonstrating the effects of thrust-vectoring systems. The PEV are separate from the nozzle, so a conventional axisymmetric nozzle could be used without reducing nozzle performance or adding complicated, costly vane cooling.

Postexit Vanes

From a study by B. Berrier and M. Mason, it was found that the postexit vanes were competitive with other multiaxis, nonaxisymmetric systems even though large losses were incurred (ref. 21). In addition, spoon-shaped vanes were more effective than single-curvature vanes. On the other hand, single-curvature vanes were more efficient than flat vanes. The type of nozzle used is of little effect on the postexit vane performance; therefore, for this study, the standard F-16 aircraft nozzle can be used. The research also showed that using four vanes rather than three provides a larger thrust envelope (fig. 2). Berrier and Mason's study also confirmed the results for the F/A-18 HARV that increasing vane area relative to the nozzle exit area increases the resultant thrust vector angle (fig. 3).

The F/A-18 project has conducted static performance testing of the postexit vanes at the NASA Langley 14 × 22 ft subsonic tunnel (ref. 22). The three-vane configuration was chosen to conform with the aftbody structure and resulted in two differently sized vanes at three different relative angles (figs. 4 and 5).

The vanes were tested at both maximum afterburner and military power and were positioned at the following angles: −10, −5, 0, 5, 10, 15, 20, 25, and 30 deg; however, the F/A-18 HARV vane-deflection angle is structurally limited to 25°. The test results were compiled and used to draw correlations for the size and position of the thrust vectoring system to be used in this study (appendix B).

The TVCS vane for the F-16 aircraft in this study was chosen to use highly effective, double-curvature vanes, the same as used on the F/A-18 HARV. The F-16 aircraft will employ a convergent-divergent standard nozzle. In addition, the four vanes will be placed symmetrically on the aftbody for a larger control envelope and simpler control system than a three-vane configuration permits (fig. 2). From the results of the F/A-18 HARV static tests, correlations between the jet deflections, efficiency, and direction with thrust vectoring control deflection were made to predict the performance characteristics of the F-16 aircraft.

Figures 3 and 6 show that for single-vane deflections the larger the vane area, the greater the thrust deflection. In addition, the maximum afterburner power setting is more effective than the military power setting for vane deflections between 10 and 25° (figs. 3 and 6). Nozzle pressure ratios significantly increase the thrust deflections, especially at smaller vane-deflection angles. This increase occurs because

10

of the expanded flow contacting the vanes at smaller deflections (fig. 7). The maximum NPR effects occur from 15 to 25° for military power and 10 to 15° for maximum afterburner with NPRs of 5 and 6 having the greatest differences.

The two-vane deflections have more vane area relative to the nozzle exit area and, therefore, have greater thrust deflections compared to single vanes. It was found, however, that significant interference effects occurred in large deflections and were highly dependent on power settings, vane sizes, positions, and deflections. Figure 8 shows that the A and C vane configurations, which are positioned 138.5° apart, resulted in less thrust deflection than the smaller B and C vane area combination, showing the importance of relative angle to vane interference. In figures 9 and 10, it is seen that vane interference increased with nozzle pressure ratio and that all vane configurations were affected. Comparison of figures 8 and 10 with figures 11 and 12 reveals that the interference effects for maximum afterburner power are greater than the military power setting and effectiveness decreases further with nozzle pressure ratio. The two vanes deflected the jet far enough to impinge the jet on the inactive vane therefore eliminating further jet deflection and incurring high losses. At higher nozzle pressure ratios with the flow expanding as it leaves the nozzle, the jet-deflection performance was further reduced. Figure 12 shows that vane size and position have a major effect on jet deflection and interference. Note that inactive vane position, size, and deflection played a role in interference.

The proposed F-16 aircraft would use the standard HARV TVCS because of the availability of the data. Future designs should incorporate asymmetric vane deflections for opposite vanes or position the inactive vane farther from the nozzle so as not to impinge on the vectored engine thrust. Either configuration would reduce interference and increase jet-off effectiveness.

The direction of the vector for the vanes reacted as expected. When a vane at a specified radial position is deflected, the thrust vector radial direction should be opposite the vane radial position. For very small values of total vane deflection, the readings produced very small vector deflections and showed considerable error. On the other hand, as the vane deflection increased to 15°, where deflection becomes significant, the radial directions approached the expected angle (fig. 13). Similar correlations can be found in the case of two vanes deflecting at once. The direction is a function of vane radial position and radial vane size. When both vanes have the same deflection angle, for example,

$$\Omega_{vector} = \frac{ARC_1\,\Omega_1 + ARC_2\Omega_2}{ARC_1 + ARC_2}$$

where

$$ARC = \text{radial vane size}$$
$$\Omega = \text{radial vane position angle}$$

This equation assumes that similar vanes are used, and there is no third-vane interference.

The efficiency of the postexit vanes is the total magnitude of the deflected thrust vector over the magnitude of the undeflected thrust vector. Efficiency for TVCS vanes is poor when the vanes are deflected beyond 20° (figs. 14 and 15). In figures 16 and 17, the smaller area B and C vane

combination is slightly more effective than the other combinations, and there is a crossover of efficiency with nozzle pressure ratios because of inactive vane interference. The nozzle pressure ratio decreases efficiency slightly, and the maximum afterburner case is substantially more efficient than the military power setting.

The efficiency and deflection of the postexit vane thrust vectoring system is highly dependent on active and inactive areas, placement, vane deflections, and nozzle pressure ratios. The maximum afterburner configuration has the greater deflections, efficiencies, and interference effects compared to the military power setting.

Thrust Vectoring Simulation

The thrust vectoring simulation subroutines used to determine the deflection, direction, and efficiency are based on the thrust vectoring data from the F/A-18 HARV cold-jet tests. The single-vane thrust deflections curves with respect to the vane deflections were approximated using fourth-order polynomials at each nozzle pressure ratio for both military power and maximum afterburner. The efficiency correlations with respect to the single vane deflections used third-order approximations. The two vane, equal deflection results are modified single vane deflection models which account for the interference of two differently sized vanes at a relative radial angle. The vane-deflection and efficiency-correlation programs are reasonable approximations within the angles, deflections, and sizes of the F/A-18 HARV configuration. Better results for single-vane deflections are achieved because the correlation programs were directly interpolated from the single-vane data, and no interference effects were present.

The F-16 radial vane width of 60° was based on the F/A-18 HARV ratio of vane radial width to that of the total radial degrees. Vane relative angles of 90° were chosen to simplify control laws, obtain maximum effectiveness and efficiency, allow vane placement without restricting horizontal tail and rudder deflections, and gain maximum thrust vectoring in pitch or yaw with two equal vane deflections.

Aircraft Configuration

The F-16 fighter used for the study incorporated an F-100 EMD engine with DEEC control. Four Inconel, double curvature, postexit vanes were positioned at ±45° and at ±135° for pure pitch or yaw vectoring with two vane deflections (fig. 4). The vane control power was derived from linear interpolation of two equal-vane deflections of 20° assuming that the vane-zero position was at 0° vane deflection. The vane deflection, direction, and efficiency models are based on the F/A-18 HARV and assume no differential vane deflections and no control surface limiters. The leading-edge-flap schedule for the F-16 aircraft was used, but the horizontal tail was untrimmed and at 0° deflection. The c.g. positions are maintained at 30 percent of the mean aerodynamic chord for all configurations. The weights and inertias are as follows:

$$W_{t_0} = 16,330 \, \text{lb}$$

$$I_{xx_0} = 9,470 \, \text{slug/ft}^2$$

$$I_{yy_0} = 49,450 \, \text{slug/ft}^2$$

$$I_{zz_0} = 56,760 \text{ slug/ft}^2$$

$$I_{xz_0} = 310 \text{ slug/ft}^2$$

From Nicolai (ref. 23) the weight of a vertical stabilizer for a conventional aircraft with subsonic and supersonic capabilities is

$$W_{t_{vt}} = 0.19\gamma^{1.014}$$

$$\gamma = \left(1 + \frac{h_{ht}}{h_{vt}}\right)^{0.5} (W_{t_0}n)^{0.363}(S_{vt})^{1.089}M_{max_{s.l.}}{}^{0.601}L_{vt}$$

$$\left(1 + \frac{S_r}{S_{vt}}\right)^{0.217} AR_{vt}{}^{0.337}(1 + \lambda_{vt})^{0.363}(\cos \Lambda_{\dot r})^{-0.484}$$

With the following results, the weights for the vertical tail and two ventral fins are

$$W_{t_{vt}} = 300 \text{ lb}$$

$$W_{t_{\text{ventral fins}}} = 106 \text{ lb}$$

where $\frac{h_{ht}}{h_{vt}} = 0$ for a fuselage-mounted horizontal tail. The weights for the proposed F-16 TVCS and counterbalance are $W_{t_{TVCS}} = 600$ lb and $W_{t_{cb}} = 600$ lb. The inertias are defined as follows:

$$I_{xx} = \int (y^2 + z^2)\delta m$$

$$I_{yy} = \int (x^2 + z^2)\delta m$$

$$I_{zz} = \int (x^2 + y^2)\delta m$$

$$I_{xz} = \int (xz)\delta m$$

$$I_{xy} = I_{yz} = 0$$

$$I_{yy_{tv + cb}} = 14,906 \text{ slug/ft}^2$$

$$I_{zz_{tv + cb}} = 14,906 \text{ slug/ft}^2$$

$$I_{xx_{vt\ 100\%}} = 84 \text{ slug/ft}^2$$

$$I_{yy_{vt\ 100\%}} = 3,143 \text{ slug/ft}^2$$

$$I_{zz_{vt\ 100\%}} = 2,387 \text{ slug/ft}^2$$

$$I_{xz_{vt\ 100\%}} = 559 \text{ slug/ft}^2$$

The reduction of tail height was assumed to be proportional to the reduction in the vertical tail weight.

AERODYNAMIC PRELIMINARY ANALYSIS SYSTEM

To obtain the coefficients for the F-16 aircraft flight envelope, the Aerodynamic Preliminary Analysis System II (APAS) was used. The APAS is a computer code on the NASA timesharing network that uses a unified distributed panel method and incorporates potential flow theory with edge considerations at subsonic and supersonic speeds in the analysis of three-dimensional configurations having multiple nonplanar surfaces of arbitrary platform and of bodies of noncircular contour. These surfaces are analyzed statically, rotary, and longitudinally. Then, longitudinal and lateral-directional characteristics are derived. In preliminary design, the finite-element analysis combined with realistic assessments of its limitations, is a valuable tool (ref. 24).

The jet-flap and jet-interference effects options on APAS were not used because of inoperability. As a result, the F-16 aircraft intake was faired in for the APAS configuration (fig. 18), and the effects of unvectored engine thrust were assumed to be small. Singularities in the system occurred when operating at Mach numbers 1.0 and 1.2. As a result, the aerodynamic data were taken at Mach numbers 0.2, 0.4, 0.6, 0.8, 0.9, 1.1, 1.25, 1.4, 1.6, and 1.8. For this study, the c.g. position was assumed to be at 30 percent of the mean aerodynamic chord at the frontmost position of the c.g. envelope for the F-16 aircraft.

Stability Coefficients

One objective of this study was to examine the effects of reducing the vertical tail size on aircraft stability and control. The five configurations that were studied with the APAS code are presented in figure 18. The APAS studies produce stability coefficients that followed the expected trends with respect to Mach number for all but low supersonic speeds (refs. 25 and 26). The variations of the yawing moments, rolling moments, side forces with sideslip angle, and roll and yaw rates showed a decrease in the magnitude of the coefficients as tail size was reduced (figs. 19 to 30). The large increases in the coefficients at Mach numbers 1.1 through 1.4 were much larger than expected and are considered to be in error.

As was expected, directional stability decreased as the tail size was reduced. Directional stability and rudder control power were reduced by 35 percent with configuration B and 70 percent for configuration C (fig. 19). The aircraft appears to have become statically unstable, $C_{n_\beta} < 0.0$, between 20 and 30 percent tail height. Although the magnitudes of the lateral-directional stability coefficients do not match well with those presented in a study of the prototype F-16 and the F-16 aircraft with the c.g. at 35 percent (refs. 26 and 27), the ratios of the coefficients must be accurate for the linear perturbation analysis to be correct.

The longitudinal coefficients for the baseline aircraft were very similar to those expected; but, when the tail size was reduced, some uncharacteristic variations occurred. The longitudinal coefficients should have remained the same; however, in the lateral-directional analysis of APAS, a small longitudinal variation error occurs (figs. 31 and 32). Because the longitudinal characteristics are of secondary concern for the small perturbation analysis and are only used to obtain the lift coefficient, the results are considered acceptable. For the stability analysis of the F-16 aircraft, the 100 percent vertical tail

14

configuration was used for all longitudinal coefficients. Comparison of lift slope coefficients between APAS at 30 percent c.g. and wind and water tunnel models at 35 percent c.g. reveals an average difference of 8 percent (ref. 28).

Vertical Tail Considerations

The vertical tail provides directional stability and control and must be designed to accommodate safe operations such as high- and low-speed flight, takeoffs and landings in crosswinds, one-engine-out stability, high angle-of-attack flight, and recovery from spins. Supersonic directional stability is a result of small differences in the tail surfaces and fuselage stability characteristics. For high-speed flight, the fuselage stability characteristics do not change; however, the vertical tail surfaces may have decreased effectiveness because of elastic deformations and become critical at higher Mach numbers (ref. 29). This problem is accentuated at high angles of attack and at both subsonic and supersonic flight. The F-16 aircraft has an all-moving horizontal tail and two ventral fins; however, the APAS and stability analysis codes used in this study do not account for the aeroelastic effects caused by high-speed flight.

Since supersonic planes fly at high altitudes, the stability derivatives become increasingly ineffective as air density decreases, and the inertial effects become more important. The stability of the aircraft depends on the parameters $\frac{C_{n_\beta}}{I_{xx}}$ and $\frac{C_{n_\beta}}{I_{zz}}$. Since C_{n_β} decreases with increasing Mach number, larger tail areas, or an artificial substitute are required. Because the postexit vane thrust vectoring system adds more mass and inertia to the aircraft than the reduction in tail size, these effects become a further decrease in high-speed directional stability.

TVCS Aerodynamic-Induced Results

For axisymmetric and nonaxisymmetric all-moving nozzles, there was found to be no aerodynamic cross coupling of control forces or moments (ref. 30). For postexit vanes, however, at low vane and low jet-deflection angles, there were large discrepancies in the jet direction because of the very small values of vane forces (fig. 12). Interference effects between the vanes and vane structural bending are other factors which may have caused small amounts of error in jet direction. For the model employed for this study, it was assumed that there was no cross coupling between the thrust vectoring control vanes.

From the studies done for the F/A-18 HARV project conducted at the NASA Langley 30 × 60 ft wind tunnel on a 16 percent model of the F/A-18, the induced aerodynamic effects of the TVCS were obtained (ref. 22). Drag and lift were decreased by vectoring up and increased by vectoring down as expected. These changes are analogous to a blown flap, increasing lift with blowing down and, thereby, increasing induced drag. Similar results for lateral-directional vectoring were observed. The TVCS-induced effects for the F-16 aircraft have values that are less than 4 percent of the magnitude of the yawing moment and side force stability coefficients at Mach 0.2 and at 15° angle of attack. The correlations between wing area, wing span, number of engines, and number and size of vanes were used between the F-16 and F/A-18 aircraft (appendix B).

Jet-off effects of postexit vane deflections are significant for differential vane deflections. Although these effects are not incorporated in the F/A-18 HARV or in this study, such jet-off effects should be considered for future thrust vectoring aircraft research. The postexit vanes act as aerodynamic surfaces

such as rudders, elevators, or speed brakes. The differential deflections of thrust vectoring vanes will eliminate losses caused by interference and increase the control power available since the vane area can be 25 percent of that for the rudder.

Drag Effects

The largest drag penalties at transonic speeds result from the effects of the horizontal and vertical tail surfaces. On studies of the F-15 S/MTD model, removing the vertical and horizontal tails reduced the overall drag from 15 to 16 percent, while vertical tail removal alone resulted in a 10 percent drag reduction in the transonic regime. Slightly more than half of the drag reduction was because of the skin friction drag, and the rest was because of the adverse interaction with the aftbody (ref. 17).

As expected for the APAS results, the aircraft drag reduced proportionally as tail size was reduced. The largest drag reductions for APAS were made in the skin friction drag (fig. 33). A 14.5 percent reduction in skin friction drag occurs in the removal of the vertical tail and ventrals. An 11.3 percent reduction occurs with removal of the vertical tail. The wave, base, and vortex drags are relatively unaffected by the change in tail size. Total drag values at Mach 1.1 and Mach 1.25 appear to be much larger than wind tunnel results and are considered to be in error.

The drag coefficients were calculated at 0° angle of attack with no surface deflections and, therefore, do not include the trim drag, the drag caused by control surfaces, or the unvectored jet-induced drag. Skin friction drag can be reduced by removing the vertical tail. Since skin friction drag accounts for a little more than half the drag caused by the tail, higher drag savings could be expected. By removing the vertical tail, substantial drag reduction could be achieved if drag as a result of the TVCS is not significant. Drag increase because of the postexit vanes hardware for 0° angle of attack and 0° horizontal tail deflection is calculated to be 0.0027. For the F-16 aircraft, this increase is 13 percent of the minimum drag at Mach 0.2 and 6 percent at Mach 1.8.

The drag penalties of the postexit vanes control system, benefits of the reduction of tail size, and optimal pitch vectoring for a trimmed aircraft must be compared to determine the performance gains of the aircraft. In this case, because the APAS drag results are not considered accurate enough for a proper comparison, these calculations were not performed.

Spinning

There are two areas in which thrust vectoring could help eliminate the danger of spins: spin resistance and control power. Spin resistance is the susceptibility to spiral with and without rolling inputs and has significant impact on the handling of the aircraft (ref. 23). The following equation describes the region of spin susceptibility for nonrolling turning maneuvers without lateral-directional inputs:

$$C_{n_{\beta_{\text{dynamic}}}} = C_{n_\beta} - C_{\ell_\beta} \frac{I_{zz}}{I_{xx}} \tan \alpha$$

A negative $C_{n_{\beta_{dynamic}}}$ indicates spin susceptibility. For accessing the spin susceptibility in turning maneuvers where lateral-control inputs are introduced, the following lateral coefficient spin parameter (LCSP) is employed:

$$\text{LCSP} = C_{n_\beta} - C_{\ell_\beta}\frac{C_{n_{\delta a}}}{C_{\ell_{\delta a}}}$$

For a more detailed discussion of LCSP, see reference 23. When the vertical tail size is reduced, at high angles of attack or at high Mach numbers, directional stability of the aircraft, C_{n_β}, decreases; therefore, susceptibility in both the parameters increases. Thrust vectoring control for yaw will not be beneficial in improving the LCSP; however, a twin-engine aircraft with thrust vectoring for roll control will improve the resistance parameter for rolling maneuvers. A suggested modification for the LCSP parameter could be

$$\text{LCSP} = C_{n_\beta} - C_{\ell_\beta}\left(\frac{C_{n_{\delta a}}}{C_{\ell_{\delta a}}} + \frac{C_{n_{\delta TVCS}}}{C_{\ell_{\delta TVCS}}}\right)$$

Since thrust vectoring roll would not induce any yawing moment unless there was a relationship similar to the rudder and aileron interconnect, yawing moment caused by thrust vectoring would have no effect on spin stability. For a single-engine aircraft, such as the F-16, this multiengine characteristic would not be a benefit. Relaxing the stability of the aircraft by decreasing the vertical tail size to approximately 25 percent of its original height will decrease the spin resistance parameters to zero. These resistance parameters represent the spin susceptibility of an aircraft without the additional stability resulting from control systems with rate and acceleration feedbacks.

The rudder is the traditional control surface to be employed in a spin to stop aircraft rotation; however, careful attention must be paid to the design and placement of the horizontal and vertical tail surfaces to ensure that the rudder will be effective. During a spin, the vertical tail surface can be made ineffective by the disturbed flow from the wing and horizontal tail. Since thrust vectoring depends on engine settings and not on the aftbody flow field of the aircraft, the potential thrust vectoring control power will be nearly constant. In addition, the pilot may have the ability to fly in this regime with such control as to never enter an unintended spinning state.

Angle-of-Attack Considerations

For the F-16 aircraft, static lateral-directional stability remains positive for all angles of attack within the limiter boundary of 29°. Directional stability was high below an angle of attack of 20°, decreased to one-fourth of its initial value at 26°, and became neutral at an angle of attack of 28° (ref. 2). For this study, the angle of attack was never assumed greater than 20° for steady-level flight (fig. 34). The importance of yaw and pitch vectoring power with increasing angle of attack is that the required control power grows exponentially for a given roll rate (ref. 8).

The change in angle of attack requires that the values for inertia be transformed to the correct axis (ref. 31). For example,

$$\begin{Bmatrix} I_{xx} \\ I_{zz} \\ I_{xz} \end{Bmatrix} = \begin{bmatrix} \cos^2\alpha & \sin^2\alpha & -\sin 2\alpha \\ \sin^2\alpha & \cos^2\alpha & \sin 2\alpha \\ \frac{1}{2}\sin 2\alpha & -\frac{1}{2}\sin 2\alpha & \cos 2\alpha \end{bmatrix} \begin{Bmatrix} I_{xx_0} \\ I_{zz_0} \\ I_{xz_0} \end{Bmatrix}$$

The changes that occur in the inertias with the angle-of-attack variation are seen in figure 34.

Comparisons of Vertical Tail Sizes to TVCS

The most accurate way to compare the control effectiveness of the thrust vectoring with the vertical tail is by calculating the yaw force and yawing moment coefficients. In this case, total net thrust of the airplane is defined as $T_{net} = T_{gross} - D_{ram}\cos\alpha$. For Mach numbers less than 0.4 to 0.5, the ram drag is small leaving $T_{net} \approx T_{gross}$. Since the amount of thrust vectoring available to the pilot during steady-state flight is limited to the net thrust output by the engine and equal to the drag of the aircraft, an appropriate measure of thrust vectoring power can be derived assuming that the Mach number < 0.4 to 0.5 and at small angles of attack (ref. 15). If $D = T\cos\alpha$, then $T = \frac{D}{\cos\alpha}$. Deriving the yaw force and yawing moment yields

$$Y_{\text{TVCS}} = T_{net}\sin\delta_{tv} = \frac{D\sin\delta_{tv}}{\cos\alpha}$$

likewise,

$$N_{\text{TVCS}} = T_{net}\ell_{\text{TVCS}}\sin\delta_{tv} = \frac{D\ell_{\text{TVCS}}\sin\delta_{tv}}{\cos\alpha}$$

Converting the yaw force and yawing moments into coefficients gives

$$C_{y\text{TVCS}} = \frac{Y_{\text{TVCS}}}{\bar{q}Sb} = \frac{T_{net}\sin\delta_{tv}}{\bar{q}Sb} = \frac{D\sin\delta_{tv}}{\bar{q}Sb\cos\alpha}$$

Similarly,

$$C_{n\text{TVCS}} = \frac{N_{\text{TVCS}}}{\bar{q}Sb} = \frac{T_{net}\ell_{\text{TVCS}}\sin\delta_{tv}}{\bar{q}Sb} = \frac{D\ell_{\text{TVCS}}\sin\delta_{tv}}{\bar{q}Sb\cos\alpha}$$

Converting the drag and thrust to coefficient form yields

$$C_{y\text{TVCS}} = \frac{Y_{\text{TVCS}}}{\bar{q}Sb=C_T\sin\delta_{tv}} = \frac{C_D\sin\delta_{tv}}{\cos\alpha}$$

likewise,

$$C_{n\text{TVCS}} = \frac{N_{\text{TVCS}}}{\bar{q}Sb} = C_T\ell_{\text{TVCS}}\sin\delta_{tv} = \frac{C_D\ell_{\text{TVCS}}\sin\delta_{tv}}{\cos\alpha}$$

At high angles of attack and at high Mach numbers, the thrust vectoring, yawing moment, and force coefficient equations must be defined as functions of the gross thrust. The yawing force and moment coefficients in terms of gross thrust are derived as follows:

$$Y_{\text{TVCS}} = T_{gross}\sin\delta_{tv}$$

likewise,

$$N_{\text{TVCS}} = T_{\text{gross}} \ell_{\text{TVCS}} \sin \delta_{tv}$$

and,

$$C_{y_{\text{TVCS}}} = \frac{Y_{\text{TVCS}}}{\bar{q}Sb} = \frac{T_{\text{gross}} \sin \delta_{tv}}{\bar{q}Sb} = C_{T_{\text{gross}}} \sin \delta_{tv}$$

Similarly,

$$C_{n_{\text{TVCS}}} = \frac{N_{\text{TVCS}}}{\bar{q}Sb} = \frac{T_{\text{gross}} \ell_{\text{TVCS}} \sin \delta_{tv}}{\bar{q}Sb} = C_{T_{\text{gross}}} \ell_{\text{TVCS}} \sin \delta_{tv}$$

For this study, the flight control power was determined for three cases: maximum afterburner, military power, and steady level flight. The steady level flight control power was determined for all Mach numbers and altitudes by calculating aircraft drag and then interpolating for the gross thrust from the F-100 EMD data assuming the net thrust equalled the drag.

The control power of postexit vanes compared to that of the rudder control power is presented in figures 35 and 36. In figure 35, the sea level yawing moment available with thrust vectoring is very small compared with rudder for the majority of the speed regime except at Mach 0.2, where thrust vectoring power is nearly double that of rudder. The yawing moments at 40,000 ft are much smaller than at sea level, but thrust vectoring constitutes a much larger proportion of the total control power (fig. 36). The magnitudes of the rudder and thrust vectoring control powers at 40,000 ft and at low speed represent the maximum available control power. In this case, it is assumed that the vertical tail is not affected by the high angle of attack and that the engine is at maximum afterburner. It is concluded that the thrust vectoring control power is more effective, especially at the higher thrust settings, at the higher altitudes, and at the lower speeds where the dynamic pressure is low.

For steady-state flight, when vectoring occurs, a decrease in forward thrust also occurs. This decrease is to a function of the thrust deflection angle and vectoring efficiency. The decrease is transitory and comparable to the drag and deceleration induced when the rudder deflects for directional control. As a result, for no compensation in net or gross thrust is made during the stability analysis.

STABILITY ANALYSIS USING SMALL PERTURBATION THEORY

Dynamic stability and control depends on the aerodynamics, mass and inertia, thrust characteristics, and flight conditions of the aircraft. Small linear perturbation theory was used to analyze the effects on the lateral-directional characteristics when thrust vectoring was incorporated with various tail sizes.

Small perturbation theory mathematically defines the aircraft response as the change of time of the motion variables relative to a steady-state flight condition caused by an external or internal disturbance (ref. 31). The success of the small perturbation theory is caused by the fact that many aerodynamic forces are linear functions of disturbances, and disturbed flight of considerable violence can occur with small values of linear or angular disturbance velocity (ref. 32). The derivation of the linear perturbation equations is presented in appendix A.

Engine Thrust Setting Considerations

Three control power settings were used in this study. These settings include maximum afterburner, military power, and steady level flight thrust. For all but the specific speeds, maximum afterburner and military power thrust settings would cause substantial accelerations in the forward direction and pitch attitude. This acceleration would imply violation of the small perturbation theory assumption of steady level flight. On the other hand, using the maximum afterburner control power at all flight settings would be representative of the maximum available control power. Small perturbation theory states that the total velocity is the sum of the steady state and disturbance velocities. The disturbance velocity can be considered the disturbance acceleration multiplied by an increment of time. If the increment of time becomes infinitely small, then the disturbance velocity also becomes infinitely small. Then, looking at the small perturbation results for maximum afterburner and military power settings at all speeds is representative of the maximum available control power at an instantaneous time t or an increased control effectiveness when compared to steady-state thrust. Observing the effect of increased control effectiveness of postexit vanes at maximum afterburner would be indicative of the effects of an increased ratio of vane to rudder deflection scheduling or the increased effectiveness of an axisymmetric balanced beam pitch/yaw vectoring nozzle.

The differences in thrust vectoring control power because of engine thrust setting for 40,000 ft are shown in figure 37. At the lower and higher Mach numbers, the control power for the steady-state flight engine setting is nearly that for maximum afterburner, especially at higher altitudes. The lower density at higher altitudes requires more thrust at slower speeds because of the increased aircraft trimmed attitude. For most of the frequency response plots to be presented, however, the Mach number is 0.9 at 40,000 ft to show the differences in magnitude and phase because of different thrust settings.

Small Perturbation Results

The transient response characteristics from the small perturbation analysis consist of the spiral, roll, and dutch roll modes and were calculated using the STAB1 program (appendix B). The denominator of the lateral-directional transfer function of the aircraft, the characteristic equation, provides real roots that are the inverse of the roll and spiral mode time constants, while the complex roots provide the dutch roll frequencies and damping ratios (appendix A). These open-loop modes are a function of the stability coefficients of the aircraft and are not dependent on control power.

The controllability of sideslip, roll, and heading is a result of the aerodynamic or thrust vectoring control power and is located in the numerators in the aircraft open-loop transfer functions. The open-loop transfer functions are $\frac{\beta(s)}{\delta(s)}$, $\frac{\phi(s)}{\delta(s)}$, and $\frac{\Psi(s)}{\delta(s)}$. Like the denominator of the transfer function, the characteristic equation, roots of the numerators provide time constants, while the complex roots provide the frequencies and damping ratios (refs. 31 and 32).

When comparing the open-loop APAS results with those obtained from YF-16 aircraft flight tests, there was a very close correlation at Mach 0.2 for the dutch roll frequency and the roll time constant (refs. 26 and 27). The dutch roll damping and heading time constant did not match with those of the YF-16 aircraft. This difference would be expected because these numbers are usually very small and hard to predict. The results of the stability analysis followed the general trends when compared with

20

altitude and Mach number flight test data. As the Mach number increased, so did the differences between the STAB1 results and the real F-16 aircraft. Because the open-loop flying qualities are different than those of the real F-16 aircraft with feedback loops, this study is only a qualitative investigation of the trends associated with thrust vectoring and not a quantitative study. The effects on the aircraft caused by the additional mass and inertia, the changes in altitude and speed, the addition of thrust vectoring yaw power to the rudder control power, and the decrease of tail size are presented in figures 38 through 64.

Thrust Vectoring Control System Mass and Inertia

The addition of the inertia and mass of the thrust vectoring system for the baseline aircraft had an effect on the aircraft characteristics. The rolling and spiral modes were not significantly affected by the TVCS addition (figs. 38 and 39). The dutch roll frequency at lower speed was not affected by the changes in masses and inertias. As the speed increased, however, the frequency steadily decreased to 11 percent at Mach 1.8. In addition, the dutch roll damping increased with low speed and decreased with higher speeds as shown in figures 40 and 41. The bank angle frequency, like the dutch roll frequency, was also affected by the addition of the thrust vectoring control system (fig. 42).

Altitude

There are large changes in the flying characteristics because of the increase in altitude for the characteristic equation for 100 percent tail configuration with a TVCS. The spiral mode root shows a very small increase in magnitude at higher Mach numbers cause by altitude that indicates a decrease in the time constant (fig. 43). The roll stability mode root markedly decreases with increasing altitude as do the dutch roll mode frequency and damping (figs. 44 to 46). The errors in the lower Mach numbers for increasing altitudes do not represent steady-state flight and the magnitudes of the spiral roots and dutch roll damping ratios are so small that they will be very inaccurate.

The open-loop frequency response plots for the aircraft show a large decrease for the magnitude measured in decibels at all frequencies for the sideslip angle transfer function. For all the response plots, the expected shift in damped natural frequency with an increase of altitude was observed. For the heading, bank-angle, and open-loop transfer functions, losses in magnitude occur at frequencies above the damped natural frequency (figs. 47 to 52) and (ref. 33).

Steady-Level Flight and Maximum Afterburner Thrust

The effects of thrust vectoring at various engine settings was investigated. The larger effects of lateral-directional thrust vectoring are at the higher altitudes and lower speeds, where the rudder control power is reduced, and at higher thrust settings, where the thrust vectoring control power is largest. At higher altitudes, the control power level for steady level flight approaches that of the maximum afterburner thrust setting for high-speed flight caused by increased thrust requirements and at the very low speeds because of the induced drag from higher angles of attack. At the mid-subsonic Mach numbers, the maximum differences in vectoring power occur (fig. 37).

Adding the steady-state thrust vectoring control power to the rudder control power for the sideslip angle, open-loop transfer function has a significant magnitude increase that is comparable to the change of magnitude from sea level to an altitude of 40,000 ft (figs. 53 and 47). Figure 54 displays that at lower frequencies there was positive shift in the phase, especially for maximum afterburner and at values above the damped natural frequency where there was no differences in phase.

The combination of the maximum afterburner thrust vectoring side force and yawing moment in addition to the rudder side force, yawing and rolling moments caused substantial decreases in the overall magnitude and a shift in phase for the heading angle frequency response (figs. 55 and 56). The addition of maximum afterburner from steady-state thrust vectoring causes the three roots of the numerator to go from two stable and one unstable to all three at the origin. This shift in roots to the origin is for maximum afterburner vectoring with rudder for configuration A and occurs throughout the entire stable speed regime. Because this phenomenon occurs at steady-state thrusts for high- and low-speed flight, careful attention must be paid to thrust vectoring for both steady-state and accelerating flight.

The primary cause of this substantial change at lower frequencies is because of the addition of the thrust vectoring yaw moment. The heading angle describes the direction of the flight path and is affected in the positive direction by the side force and in the negative direction by the yawing moment. For low frequencies, yawing moment (N) from thrust vectoring causes large decreases in the magnitude. Meanwhile, the addition of thrust vectoring side force (Y) results in increases in the magnitude. As the frequencies approach the damped natural frequency the effects are opposite, the larger yawing moment increases magnitude, and the larger side force decreases the magnitude. The large decreases in magnitude caused by the relatively small addition of thrust vectoring side force and yawing moment suggests that careful attention should be paid to heading angle response when designing for precision tracking flight maneuvers at high altitudes and at high thrust situations such as close-air formation flying and in-flight refueling.

The bank-angle frequency response was significantly affected with the introduction of maximum afterburner yaw vectoring (fig. 57). A large increase in the magnitude at lower frequencies was caused by both steady-state and maximum afterburner thrust vectoring. The differences between maximum afterburner, steady-state thrust, and rudder only controls indicate a complex relationship for the bank-angle response, especially at higher frequencies. The dip in the magnitude for the standard rudder and at steady-state thrust vectoring is caused by the open-loop transfer function acting like a aileron response with a complex root rather than a rudder response with no complex roots as the rudder and maximum afterburner thrust vectoring combination acted. This difference in the response characteristics is most evident in the phase response, where there is a difference of 180° at the higher frequencies (fig. 58). The large changes in the bank-angle response with rudder and vane deflections suggest that modifications are needed for the aileron/rudder interconnect to compensate for the vectoring effects.

Reduction in Vertical Tail Size

Aircraft designers have suggested that the installation of TVCS increases the amount of control power and allows a size reduction of the vertical tail. The size reduction of the vertical tail also decreases the lateral-directional stability of the aircraft as well as control power of the rudder thereby changing the dynamics of the aircraft. To estimate the effects of vertical tail size reduction with TVCS control

22

power, the dynamic response for the aircraft was studied with maximum afterburner and deflection thrust vectoring at 100, 75, 50, and 0 percent tail height and compared with the baseline aircraft.

The addition of thrust vectoring dramatically increases the magnitude characteristics of the sideslip transfer function (figs. 59 and 53). As expected, reduction of vertical tail height shows the natural decay of the damped natural frequency to the point where it does not exist on the unstable configuration D (figs. 59 and 60). What was unexpected was the crossover between the magnitudes of configurations B and C, where the smaller tail height of configuration C has a larger magnitude at frequencies below the damped natural frequency. The results show that there are ratios of vertical tail size to thrust vectoring control which yield greater magnitudes at specified frequency ranges for the sideslip transfer function. The reduction of vertical tail size affects the lateral-directional stability and control of the aircraft, while the TVCS adds directional control. These differences in the vertical tail and TVCS cause the disproportional changes in aircraft dynamics.

The heading angle response for the various aircraft configurations shows the expected reduction in the damped natural frequencies with the reduced tail size and no natural frequency for the unstable configuration C (figs. 61 and 62). The magnitude responses increase at lower frequencies with a reduction of tail size from configuration A to configuration C which corresponds with the responses for the reduction of a decrease of thrust as seen in figure 55. The magnitude responses crossover above the damped natural frequencies. The baseline aircraft with rudder control has the largest response. The phase responses for the heading angle show that large changes can occur with the addition of thrust vectoring control power and the reduction of tail size as the root locus shift poles from real to imaginary. Like the sideslip responses, the heading responses suggest that there are ratios of thrust vectoring control power to vertical tail size that yield higher responses at specified frequencies.

The bank-angle magnitudes and phase responses show similar characteristics to the sideslip and heading angle transfer functions (figs. 63 and 64). The complex roots in the denominator of the transfer function, which make up the damped natural frequency and damping, decrease in frequency with a decrease in tail height and are nonexistent in configuration D. The complex roots of the numerator that appear in the baseline aircraft are real roots in configuration A with thrust vectoring and are complex and increasing in frequency with a decrease in tail height. The response for lower frequency once again has crossovers and disproportional magnitudes for decreasing tail height. The large shift in phase response with the addition of TVCS to the baseline aircraft is caused by the change of the complex roots in the denominator to real roots. The complex and real roots in the numerator and denominator can significantly change the phase and magnitude characteristics of the bank-angle response.

To meet the level 1 flying qualities for a highly maneuverable fighter aircraft, certain aircraft characteristics must be maintained. The dutch roll damping and frequency, spiral mode, and bank mode change with configuration changes. Such changes are especially pronounced at high Mach numbers and altitudes (ref. 31). The dutch roll frequency must be greater than 1 rad/sec. Because reducing the tail size reduces the dutch roll frequency, especially at higher altitudes and Mach numbers, sideslip angle, yaw, and roll rate feedback loops would need to be introduced (ref. 31). The dutch roll damping, roll, and spiral mode roots can also be maintained through the use of feedback loops like those currently employed on the F-16 aircraft. Because this study did not employ these feedbacks, the exact magnitudes of the flying characteristics and the amount of tail size reduction cannot be predicted for a current flying

vehicle. Without feedback loops, tail height for an F-16 aircraft may be reduced to the difference between configurations C and D for steady-state flight and still be stable.

SUMMARY

Effectiveness and efficiency of the postexit vane TVCS are highly dependent on engine thrust setting, nozzle pressure ratio, and vane area, placement, and deflection. The large, simultaneous, two-vane deflections caused thrust deflections which forced the thrust vector to impinge on the inactive vane. In addition, the deflections caused large losses in effectiveness and efficiency. Such losses were especially pronounced at higher engine thrust settings and nozzle pressure ratios. In addition, mass and inertia increases caused by the thrust vectoring control system and counterbalance weight are much larger in magnitude than such increases for the removal of the vertical tail for a postexit vanes system.

Reduction of vertical tail size decreased the skin friction drag coefficient and stability coefficients as predicted. On the other hand, the drag and weight increases of the postexit vanes hardware eliminated the potential drag and weight reductions except for the gains to be made through use of optimum pitch vectoring.

Compared with postexit vanes, future thrust vectoring systems will have greatly improved efficiency, effectiveness, and drag and weight effects. Thrust vectoring will be a benefit of control when the aircraft is in the spin regime. Conversely, such vectoring will not affect the open-loop susceptibility of the aircraft to entering into a spin as would a reduction in the size of the vertical tail. Thrust vector becomes significant at higher altitudes and lower speeds, where the dynamic pressure is low. The thrust vectoring control power available is a function of the gross thrust and not the net thrust for all Mach numbers above 0.4 to 0.5 because of the effects of ram drag.

Adding thrust vectoring to the rudder control power and changing altitude and tail size have significant affects on the stability and control characteristics of F-16 aircraft. Meanwhile, the addition of the mass and inertia of the thrust vectoring control system has very small effects. The results presented are the open-loop transfer functions of the aircraft and do not represent the closed-loop, multiple feedback system currently employed by F-16 aircraft. It is not possible to accurately state the amount of tail size reduction. It is possible, however, to observe that the tail size of the aircraft can be reduced.

The most important parameter for observing the improved yaw characteristics is the sideslip transfer function because this function represents the power of the directional control. When incorporating maximum afterburner or steady-level thrust, significant increases in magnitude can be achieved. The differences in the frequency responses suggest that there is an optimum combination of thrust vectoring, tail size, rudder control power, and vane deflection scheduling for the highest magnitude.

The large changes in phase angles and magnitudes for heading and roll responses with relatively small increases in thrust vectoring control power or decreases in tail size suggest that careful attention should be paid to these characteristics and the integration of adding on yaw vectoring to the rudder control.

CONCLUDING REMARKS

At high altitudes, low speeds, and high engine thrust settings, thrust vectoring control can significantly increase aircraft maneuverability and spin control capabilities.

The effectiveness and efficiency of postexit vane thrust vectoring control systems are highly dependent on the engine thrust setting, the nozzle pressure ratio, and the area, placement, and deflection of the vanes.

The drag and weight reductions caused by the decrease in vertical tail size are not large enough to compensate for the increases because of the current postexit vane thrust vectoring systems. Future systems will have improved efficiency, effectiveness, drag, and weight effects to increase the performance of the aircraft.

Large disproportional changes in the magnitude and phase characteristics of the frequency response for the sideslip, heading, and bank angle transfer functions occur with the introduction of thrust vectoring and the reduction of vertical tail height.

The vertical tail height can be reduced significantly for an aircraft by using thrust vectoring; however, only through careful attention to the tail size, vectoring effectiveness, as well as vane to rudder scheduling will the optimum control and performance be obtained.

For future research, it is recommended that the effects of a more advanced axisymmetric pitch and yaw thrust vectoring nozzle design be investigated. To increase two-vane effectiveness and efficiency, it is recommended that all postexit vanes have coordinated symmetric and asymmetric deflections to eliminate jet impingement interference and to allow inactive vanes to act as aerodynamic control surfaces.

It is necessary to investigate the effects of a feedback control system to determine the amount of vertical tail height reduction allowable to maintain level 1 flying qualities. Further studies on the effects of pitch and yaw thrust vectoring control power during nonsteady-state flight conditions and nonlinear regimes, such as takeoffs, landings, high angle-of-attack flight, and maneuvering flight should be performed.

Dryden Flight Research Facility
National Aeronautics and Space Administration
Edwards, California, August 22, 1990

APPENDIX A

EQUATIONS OF MOTION

The following sum of the forces and moments are extracted from refs. 22 and 23:

$$\Sigma F_x = m(\dot{U} + QW - RV)$$

$$\Sigma F_y = m(\dot{V} - PW + RU)$$

$$\Sigma F_Z = m(\dot{W} + PV - QU)$$

$$\Sigma L = I_{xx}\dot{P} + QR(I_{zz} - I_{yy}) - I_{yz}(Q^2 - R^2) - I_{xz}(\dot{R} + PQ) - I_{xy}(\dot{Q} - PR)$$

$$\Sigma M = I_{yy}\dot{Q} + PR(I_{xx} - I_{zz}) + I_{xz}(P^2 - R^2) - I_{yz}(\dot{R} - PQ) - I_{xy}(\dot{P} + QR)$$

$$\Sigma N = I_{zz}\dot{R} + PQ(I_{yy} - I_{xx}) - I_{xy}(P^2 - Q^2) - I_{xz}(\dot{P} - QR) - I_{yz}(\dot{Q} + PR)$$

Assuming that the c.g. position is on the centerline of the aircraft

$$I_{xy} = Iyz = 0$$

$$\Sigma L = I_{xx}\dot{P} + QR(I_{zz} - I_{yy}) - I_{xz}(\dot{R} + PQ)$$

$$\Sigma M = I_{yy}\dot{Q} + PR(I_{xx} - I_{zz}) + I_{xz}(P^2 - R^2)$$

$$\Sigma N = I_{zz}\dot{R} + PQ(I_{yy} - I_{xx}) - I_{xz}(\dot{P} - QR)$$

The lateral-directional aircraft characteristic forces and moments are

$$\Sigma F_y = \left(C_{y_\beta}\beta + C_{y_p}\frac{Pb}{2U} + C_{y_r}\frac{Rb}{2U} + C_{y_\delta}\delta \right)\bar{q}S + mg\sin\phi\cos\theta$$

$$\Sigma L = \left(C_{\ell_\beta}\beta + C_{\ell_p}\frac{Pb}{2U} + C_{\ell_r}\frac{Rb}{2U} + C_{\ell_\delta}\delta \right)\bar{q}Sb$$

$$\Sigma N = \left(C_{n_\beta}\beta + C_{n_p}\frac{Pb}{2U} + C_{n_r}\frac{Rb}{2U} + C_{n_\delta}\delta \right)\bar{q}Sb$$

where δ is the control surface deflections for ailerons, rudders, and thrust vectoring.

Adding the equations of aircraft motion gives

$$m(\dot{V} - PW + RU) = \left(C_{y_\beta}\beta + C_{y_p}\frac{Pb}{2U} + \bar{q}S \ C_{y_r}\frac{Rb}{2U} + C_{y_\delta}\delta\right)\bar{q}S$$
$$+ mg\sin\phi\cos\theta$$

$$I_{xx}\dot{P} + QR(I_{zz} - I_{yy}) - I_{xz}(\dot{R} + PQ) = \left(C_{\ell_\beta}\beta + C_{\ell_p}\frac{Pb}{2U} + C_{\ell_r}\frac{Rb}{2U} + C_{\ell_\delta}\delta\right)\bar{q}Sb$$

$$I_{zz}\dot{R} + PQ(I_{yy} - I_{xx}) - I_{xz}(\dot{P} - QR) = \left(C_{n_\beta}\beta + C_{n_p}\frac{Pb}{2U} + C_{n_r}\frac{Rb}{2U} + C_{n_\delta}\delta\right)\bar{q}Sb$$

Assuming small perturbations about a reference flight condition, the velocity components can be written

$$U = U_0 + u$$
$$V = V_0 + v$$
$$W = W_0 + w$$
$$P = P_0 + p$$
$$Q = Q_0 + q$$
$$R = R_0 + r$$

where
$$V_0 = W_0 = P_0 = Q_0 = R_0 = 0$$

for steady-level flight. Assuming that the perturbations are small, the products would be approximately zero

$$m(\dot{v} + rU_0) = \left(C_{y_\beta}\beta + C_{Y_p}\frac{pb}{2U_0} + C_{y_r}\frac{rb}{2U_0} + C_{y_\delta}\delta\right)\bar{q}S + mg\sin\phi\cos\theta$$

$$I_{xx}\dot{p} - I_{xz}\dot{r} = \left(C_{\ell_\beta}\beta + C_{\ell_p}\frac{pb}{2U_0} + C_{\ell_r}\frac{rb}{2U_0} + C_{\ell_\delta}\delta\right)\bar{q}Sb$$

$$I_{zz}\dot{r} - I_{xz}\dot{p} = \left(C_{n_\beta}\beta + C_{n_p}\frac{pb}{2U_0} + C_{n_r}\frac{rb}{2U_0} + C_{n_\delta}\delta\right)\bar{q}Sb$$

Assuming $\sin\phi \approx \phi$, dividing through by the mass for the forces and inertias for moments and dimensionalizing the coefficients are as follows:

$$\dot{v} + rU_0 = g\phi\cos\theta + Y_\beta\beta + Y_p p + Y_r r + Y_\delta\delta$$

$$\dot{p} - A_1\dot{r} = L_\beta\beta + L_p p + L_r r + L_\delta\delta$$

$$\dot{r} - B_1\dot{p} = N_\beta\beta + N_p p + N_r r + N_\delta\delta$$

where the constants

$$A_1 = \frac{I_{xz}}{I_{xx}}$$

$$B_1 = \frac{I_{xz}}{I_{zz}}$$

taking the Laplace transform gives

$$(sU_0 - Y_\beta)\beta(s) - (sY_p + g\cos\theta)\phi(s) + s(U_0 - Y_r)\Psi(s) = Y_\delta\delta(s)$$

$$-L_\beta\beta(s) + \left(s^2 - L_p s\right)\phi(s) - \left(s^2 A_1 + sL_r\right)\Psi(s) = L_\delta\delta(s)$$

$$-\left(N_\beta + N_{\beta_T}\right)\beta(s) - \left(s^2 B_1 + sN_p\right)\phi(s) + (s^2 - sN_r)\Psi(s) = N_\delta\delta(s)$$

putting these equations in matrix form yields

$$\begin{bmatrix} (sU_0 - Y_\beta) & -(sY_p + g\cos\theta) & s(U_0 - Y_r) \\ -L_\beta(s) & +(s^2 - L_p s) & -(s^2 A_1 + sLr) \\ -\left(N_\beta + N_{\beta_T}\right) & -\left(s^2 B_1 + sN_p\right) & +\left(s^2 - sN_r\right) \end{bmatrix} \left\{ \begin{array}{c} \frac{\beta(s)}{\delta(s)} \\ \frac{\phi(s)}{\delta(s)} \\ \frac{\Psi(s)}{\delta(s)} \end{array} \right\} = \left\{ \begin{array}{c} Y_\delta \\ L_\delta \\ N_\delta \end{array} \right\}$$

Solving for the transfer functions yields the following relationships:

$$\frac{\beta(s)}{\delta(s)} = \frac{\begin{bmatrix} Y_\delta & -(sY_p + g\cos\theta) & +s(U_0 - Y_r) \\ L_\delta & +\left(s^2 - L_p s\right) & -\left(s^2 A_1 + sLr\right) \\ N_\delta & -\left(s^2 B_1 + sN_p\right) & +\left(s^2 - sN_r\right) \end{bmatrix}}{\begin{bmatrix} sU_0 - Y_\beta) & -(sY_p + g\cos\theta) & s(U_0 - Y_r) \\ -L_\beta(s) & +(s^2 - L_p s) & -\left(s^2 A_1 + sLr\right) \\ -\left(N_\beta + N_{\beta_T}\right) & -\left(s^2 B_1 + sN_p\right) & +(s^2 - sN_r) \end{bmatrix}}$$

$$\frac{\phi(s)}{\delta(s)} = \frac{\begin{bmatrix} (sU_0 - Y_\beta) & Y_\delta & +s(U_0 - Y_r) \\ -L_\beta(s) & L_\delta & -(s^2 A_1 + sLr) \\ -\left(N_\beta + N_{\beta_T}\right) & N_\delta & +(s^2 - sN_r) \end{bmatrix}}{\begin{bmatrix} (sU_0 - Y_\beta) & -(sY_p + g\cos\theta) & +s(U_0 - Y_r) \\ -L_\beta(s) & +(s^2 - L_p s) & -(s^2 A_1 + sLr) \\ -\left(N_\beta + N_{\beta_T}\right) & -\left(s^2 B_1 + sN_p\right) & +(s^2 - sN_r) \end{bmatrix}}$$

28

$$\frac{\Psi(s)}{\delta(s)} = \frac{\begin{bmatrix} (sU_0 - Y_\beta) & -(sY_p + g\cos\theta) & Y_\delta \\ -L_\beta(s) & +(s^2 - L_p s) & L_\delta \\ -\left(N_\beta + N_{\beta_T}\right) & -\left(s^2 B_1 + sN_p\right) & N_\delta \end{bmatrix}}{\begin{bmatrix} (sU_0 - Y_\beta) & -(sY_p + g\cos\theta) & +s(U_0 - Y_r) \\ -L_\beta(s) & +(s^2 - L_p s) & -\left(s^2 A_1 + sLr\right) \\ -\left(N_\beta + N_{\beta_T}\right) & -\left(s^2 B_1 + sN_p\right) & +(s^2 - sN_r) \end{bmatrix}}$$

with the transient response characteristics being the denominator

$$\Delta = \begin{bmatrix} (sU_0 - Y_\beta) & -(sY_p + g\cos\theta) & +s(U_0 - Y_r) \\ -L_\beta(s) & +(s^2 - L_p s) & -(s^2 A_1 + sLr) \\ -\left(N_\beta + N_{\beta_T}\right) & -\left(s^2 B_1 + sN_p\right) & +(s^2 - sN_r) \end{bmatrix}$$

Solving this matrix reveals one root indicating neutral heading stability, one first-order root known as the spiral mode, one highly convergent root known as the rolling mode, and one slowly damped, low-frequency, oscillatory, dutch roll mode. These roots are expressed as

$$\frac{\beta(s)}{\delta(s)} = \frac{s\left[A_\beta s^3 + B_\beta s^2 + C_\beta s^1 + D_\beta\right]}{s[As^4 + Bs^3 + Cs^2 + Ds^1 + E]}$$

$$\frac{\phi(s)}{\delta(s)} = \frac{s\left[A_\phi s^2 + B_\phi s^1 + C_\phi\right]}{s[As^4 + Bs^3 + Cs^2 + Ds^1 + E]}$$

$$\frac{\Psi(s)}{\delta(s)} = \frac{s\left[A_\Psi s^3 + B_\Psi s^2 + C_\Psi s^1 + D_\Psi\right]}{s[As^4 + Bs^3 + Cs^2 + Ds^1 + E]}$$

Solving for the roots of the equation results in the following poles and zeros:

$$\frac{\beta(s)}{\delta(s)} + \frac{k_\beta\,(s + \hat{z}_1)\,(s + \hat{z}_2)\,(s + \hat{z}_3)}{(s + \hat{p}_1)(s + \hat{p}_2)\left(s^2 + 2\zeta\omega + \omega^2\right)}$$

$$\frac{\phi(s)}{\delta(s)} = \frac{k_\phi\left(s^2 + 2\zeta_\phi\omega_\phi + \omega_\phi^2\right)}{(s + \hat{p}_1)(s + \hat{p}_2)\left(s^2 + 2\zeta\omega + \omega^2\right)}$$

$$\frac{\Psi(s)}{\delta(s)} = \frac{k_\Psi\,(s + \hat{z}_1)\left(s^2 + 2\zeta_\Psi\omega_\Psi + \omega_\Psi^2\right)}{(s + \hat{p}_1)(s + \hat{p}_2)\left(s^2 + 2\zeta\omega + \omega^2\right)}$$

Placing the results in standard aircraft format

$$\frac{\beta(s)}{\delta(s)} = \frac{k_\beta\left(\frac{s}{\hat{z}_1} + 1\right)\left(\frac{s}{\hat{z}_2} + 1\right)\left(\frac{s}{\hat{z}_3} + 1\right)}{\left(\frac{s}{\hat{p}_1} + 1\right)\left(\frac{s}{\hat{p}_2} + 1\right)\left(\frac{s^2}{\omega^2} + \frac{2\zeta}{\omega} + 1\right)}$$

$$\frac{\phi(s)}{\delta(s)} = \frac{k_\phi \left(\frac{s^2}{\omega_\phi^2} + \frac{2\zeta_\phi}{\omega_\phi} + 1 \right)}{\left(\frac{s}{p_1} + 1 \right) \left(\frac{s}{p_2} + 1 \right) \left(\frac{s^2}{\omega^2} + 1 \right) \left(\frac{s^2}{\omega^2} + \frac{2\zeta}{\omega} + 1 \right)}$$

$$\frac{\Psi(s)}{\delta(s)} = \frac{k_\Psi \left(\frac{s}{z_1} + 1 \right) \left(\frac{s^2}{\omega_\Psi^2} + \frac{2\zeta_\Psi}{\omega_\Psi} + 1 \right)}{\left(\frac{s}{p_1} + 1 \right) \left(\frac{s}{p_2} + 1 \right) \left(\frac{s^2}{\omega^2} + \frac{2\zeta}{\omega} + 1 \right)}$$

It is important to note that the standard format implies that the roll and heading responses will have complex roots. On the other hand, certain configurations drive all the roots of the numerators to the real axis, and the standard form is no longer valid.

APPENDIX B

COMPUTER PROGRAMS

Postexit Vane

1. TVDAT–The 11 × 11 matrix data tables from the NASA Langley cold-jet tests for each vane, nozzle pressure ratio, and engine setting.

2. JET–A series of six programs designed to calculate the thrust deflection, efficiency, and direction for each vane, vane deflection combination, NPR, and engine setting studied. Output is in EZPLOT format.

3. MOD–A series of six programs designed to simulate the results of the JET series for deflection and efficiency of the one vane and simultaneous vane-deflection cases at various NPRs, engine settings, and vane sizes and placements. Output is in EZPLOT format.

Aerodynamic

1. APAS.GEOM–The file for the APAS II program where the F-16 aircraft geometry was input.

2. F16.OUT–Output file from the APAS run.

3. TOSS/PILE–Two series of programs that compile aerodynamic coefficients into a series of data files from the APAS output file F16.OUT. Output files are in EZPLOT format.

Engine

TOSS5–A program that compiles the thrust and NPR results from the output of the F-100 EMD SPEC for both military power and maximum afterburner at various altitude and Mach numbers into a series of data files. Data files are in EZPLOT format.

Stability

1. STAB1–A program that uses linear perturbation theory to calculate the flying characteristics and incorporates the aerodynamic coefficients from the PILE program, the engine output files from TOSS5, the induced thrust effects from windtunnel tests, and the MOD series of programs as subroutines. Most output is in EZPLOT format, while other output goes into a plotting or test format.

2. BODE–An interactive program designed to produce the magnitude and phase characteristics for the frequency response. Output is formatted for use in EZPLOT.

REFERENCES

1. *Jane's All the Worlds Aircraft 1988-89*, Jane's Information Group Inc., Alexandria, VA, 1989.

2. Wilson, Donald B. and Robert C. Ettinger, *F-16A/B High Angle of Attack Evaluation*, AFFTC-TR 79-18, Oct. 1979.

3. Pennington, T.D. and R.M. Kotarba, "F-16N Supersonic Adversary Aircraft Evaluation," *Cockpit*, April-May-June 1988, pp. 4–14. (Also available as NATC-SA-164R-87, June 1988.)

4. Hernandez, Francisco J. and Frank W. Burcham, Jr., *Flight Measured and Calculated Exhaust Jet Conditions for an F-100 Engine in an F-15 Airplane*, NASA TM-100419, 1988.

5. Gal-Or, B. and A. Rasputnis, "2-D Vectoring/Reversing Nozzles for New Fighter Engines—A Review," AIAA 87-35026, Feb. 1986.

6. Sweetman, Bill, "Agile Falcon and Hornet 2000," *Interavia*, vol. XLIII, Feb. 1988, pp. 161–164.

7. Herbst, W.B., "Supermaneuverability," *Proceedings of the Workshop on Unsteady Separated Flow*, Held at USAF Academy, Aug. 10–11, 1983, AFOSR 84-0911, 1984, pp. 1–9.

8. McAtee, Thomas P., "Agility in Demand," *Aerospace America*, vol. 26, no. 5, May 1988, pp. 36–38.

9. Scott, William B., "Air Force, NASA Conduct Tests to Define Fighter Aircraft Agility," *Aviation Week and Space Technology*, vol. 130, no. 2, Jan. 9, 1989, pp. 45–47.

10. Kandebo, Stanley W., "Modified F-15B to Demonstrate STOL, Maneuver Capability," *Aviation Week and Space Technology*, vol. 130, no. 22, May 29, 1989, pp. 44–47.

11. "Agile Sukhoi Su-27 Leads Strong Soviet Presentation," *Aviation Week and Space Technology*, vol. 130, no. 25, June 19, 1989, pp. 28–30.

12. Scott, William B., "NASA Adds to Understanding of High Angle of Attack Regime," *Aviation Week and Space Technology*, vol. 130, May 22, 1989, pp. 36–42.

13. Hienz, E. and R.Vedova, "Requirements, Definition, and Preliminary Design for an Axisymmetric Vectoring Nozzle to Enhance Aircraft Maneuverability," AIAA 84-1212, June 1984.

14. Ashley, H., "On the Feasibility of Low-Speed Aircraft Maneuvers Involving Extreme Angles of Attack," *Journal of Fluids and Structures*, vol. 1, July 1987, pp. 319–335.

15. LaFroth, R.E., *Thrust Vectoring To Eliminate the Vertical Stabilizer—To Provide Directional Stability for F-111 Aircraft While Decreasing Radar Detectability*, M.S. Thesis: AFTI/GAE/AA/79D-9, Dec. 1979. (Also available as NTIS AD-A 079852.)

16. Lok, Joris J., "Stealth-Modified F-16s in Service," *Jane's Defence Weekly*, vol. 13, no. 4, Jan. 27, 1990, pp. 133.

17. "Propulsion System Integration in High-Performance Aircraft," *Aerospace Engineering*, vol. 10, no. 9, Feb. 1990, pp. 21–25.

18. Hiley, P.E., H.W. Wallace, and D.E. Booz, "Study of Non-axisymmetric Nozzles Installed in Advanced Fighter Aircraft," AIAA 75-1316, Sept. 1975.

19. Hiley, P.E., D.E. Kitzmiller, and C.M. Willard, "Installed Performance of Vectoring/Reversing Non-axisymmetric Nozzles," AIAA 78-1022, July 1978.

20. Schnell, W.C. and R.L. Grossman, "Vectoring Non-axisymmetric Nozzle Jet Induced Effects on a V/STOL Fighter Model," AIAA 78-1080, July 1978.

21. Berrier, Bobby L. and Mary L. Mason, "Static Investigation of Post-Exit Vanes for Multiaxis Thrust Vectoring," AIAA-87-1834, June 1987.

22. Bowers, Albion H., Gregory K. Noffz, Sue B. Grafton, Mary L. Mason, and Lee R. Peron, *Multiaxis Thrust Vectoring Using Axisymmetric Nozzles and Postexit Vanes on an F/A-18 Configuration Vehicle*, NASA TM-101741, 1991.

23. Nicolai, Leland M., *Fundamentals of Aircraft Design*, METS, Inc., San Jose, CA, 1984.

24. Bonner, E., W. Clever, and K. Dunn, *Aerodynamic Preliminary Analysis System 2, Part 1—Theory*, NASA CR-165627, 1981.

25. Heffley, R.K. and W.F. Jewell, *Aircraft Handling Qualities Data*, NASA CR-2144, 1972.

26. Pape, J.K. and M.P. Garland, *F-16A/B Flying Qualities Full Scale Development Test and Evaluation—Volume 1*, AFFTC TR-79-10-VOL-1, Sept. 1979.

27. Smith, J.W., *Analysis of a Lateral Pilot-Induced Oscillation Experienced on the First Flight of the YF-16 Aircraft*, NASA TM-72876, Sept. 1979.

28. Hammett, L.N., Jr., *An Investigation of the F-16 High-Angle-of-Attack Pitching-Moment Discrepency—Final Report*, AFWAL TR-81-3107, Sept. 1981.

29. Corning, Gerald, *Supersonic and Subsonic, CTOL and VTOL, Airplane Design*, Fourth ed., G. Corning Publishing, College Park, MD, 1985.

30. Capone, Francis J. and Mary L. Mason, *Multiaxis Aircraft Control Power From Thrust Vectoring at High Angles of Attack*, NASA TM-87741, 1986.

31. Roskam, Jan, *Airplane Flight Dynamics and Automatic Flight Controls*, Roskam Aviation and Engineering Corp., Ottawa, KS, 1979.

32. Etkins, Bernard, *Dynamics of Flight—Stability and Control*, Second ed., J. Wiley and Sons, New York, NY, 1982.

33. Dorf, Richard C., *Modern Control Systems*, Fourth ed., Addison-Wesley Publishing Co., Reading, MA, 1986.
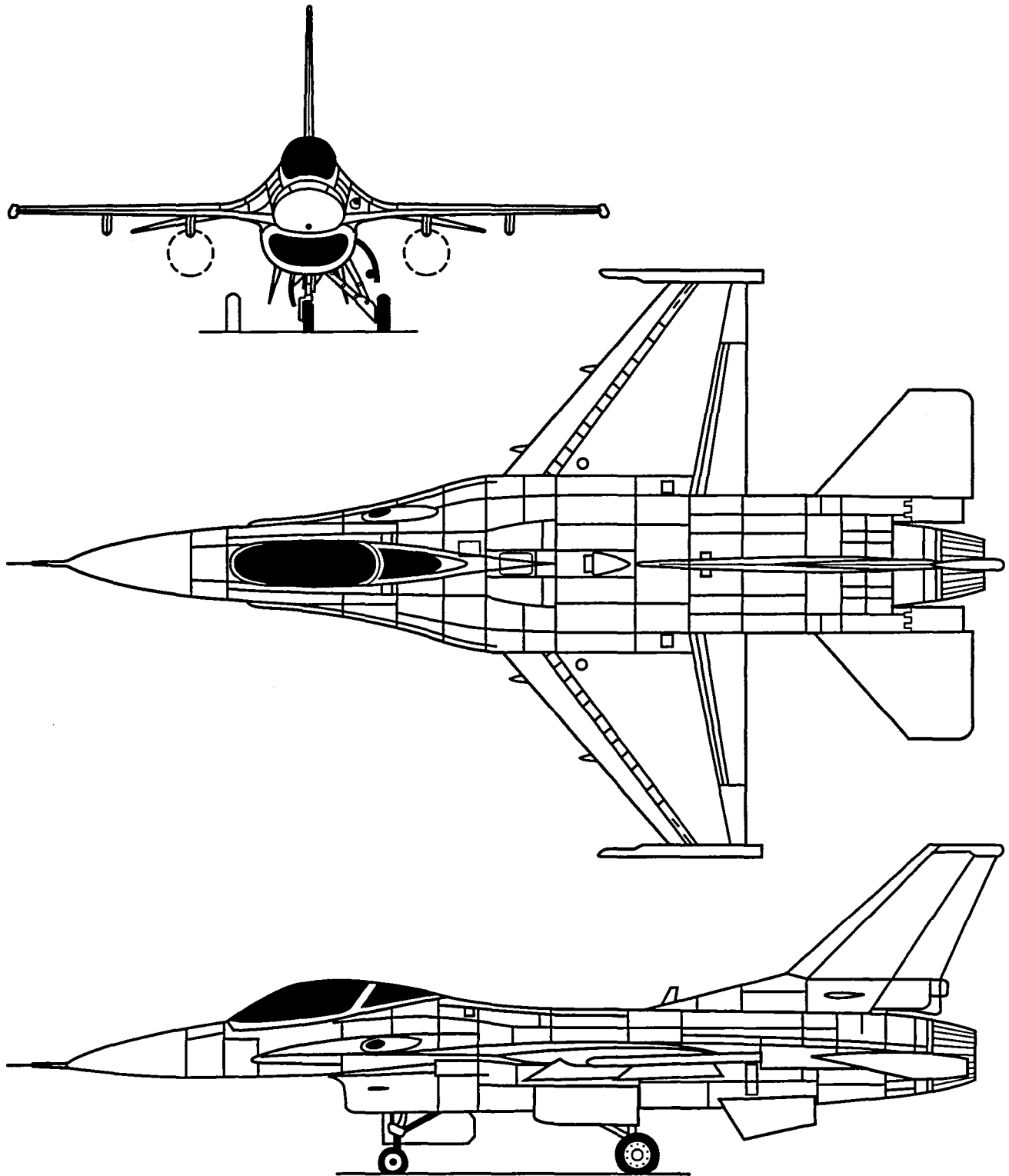
Figure 1. Three-view drawing of an F-16 Fighting Falcon.

910846
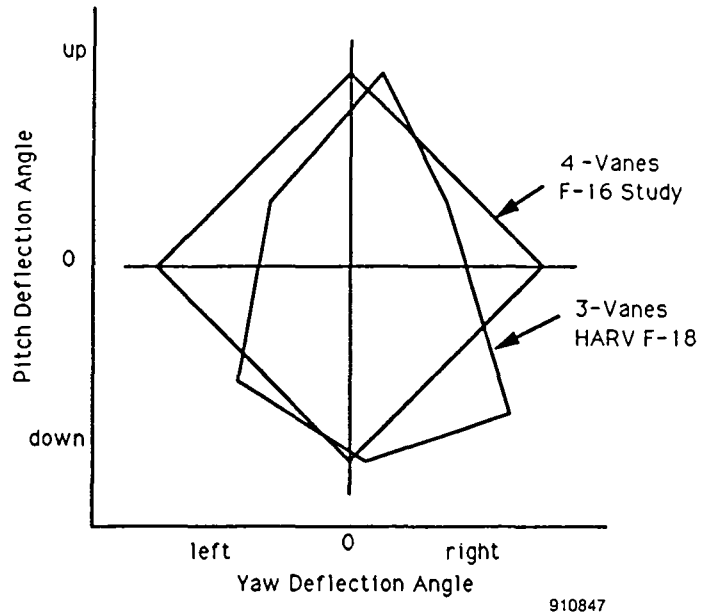
Figure 2. Thrust vector envelope for three and four vanes.
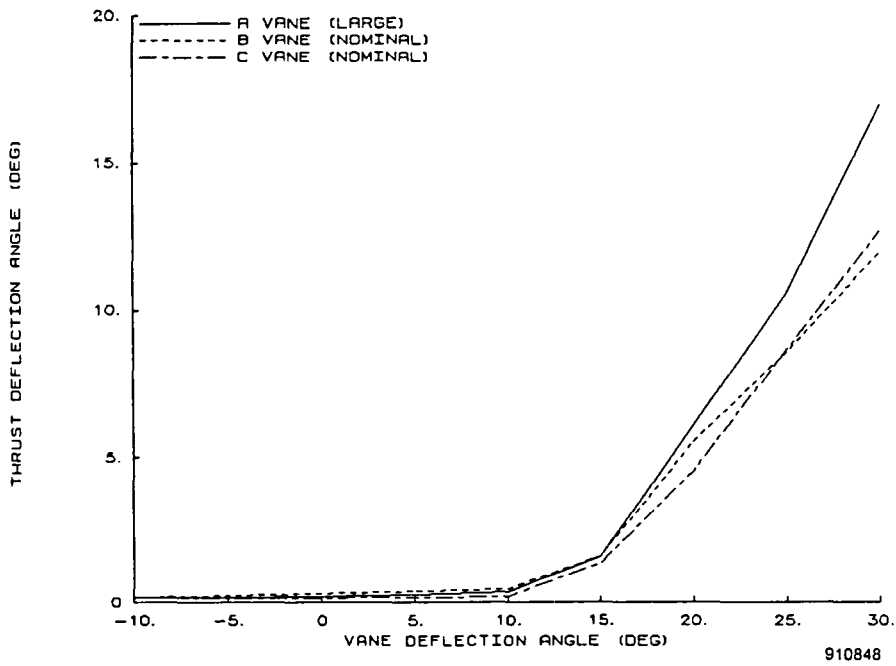
Figure 3. Single-vane deflections at military power and nozzle pressure ratio = 2.

35
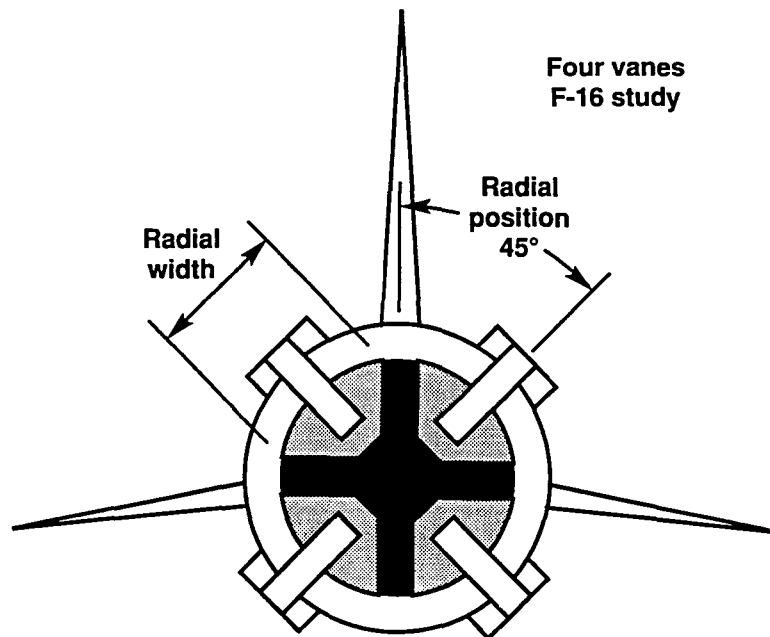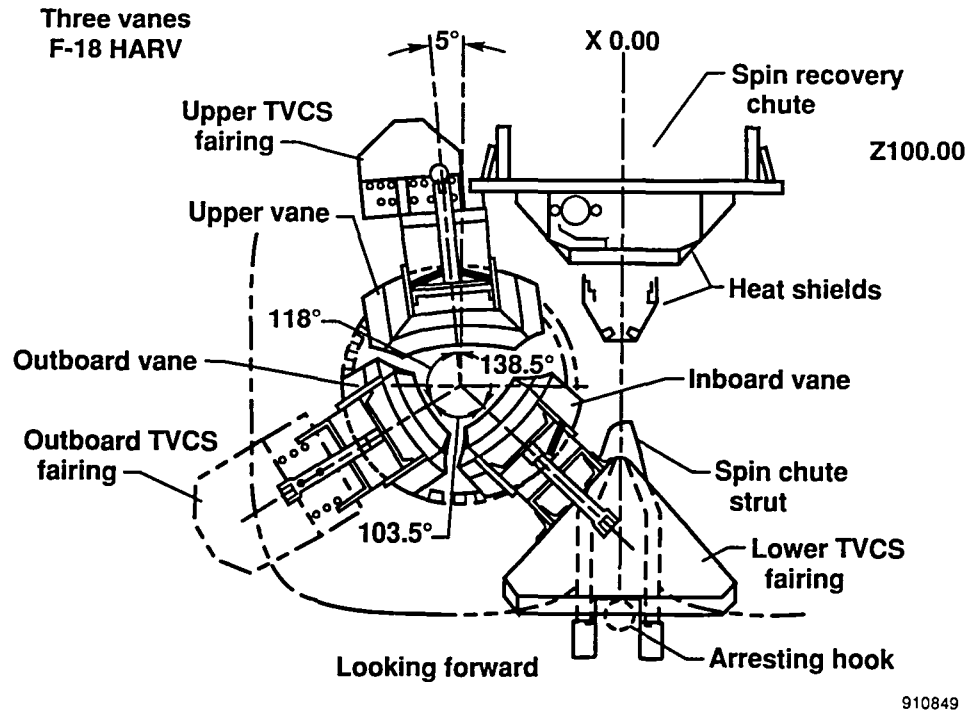
Figure 4. Three- and four-vane thrust vectoring control system arrangements.

Outboard, inboard vanes
Width – 15 in.
Length – 20 in.
Area – 262.8 in.^{2}

Large upper vane
Width – 20 in.
Length – 20 in.
Area – 359.7 in.^{2}

10°

25°

900161
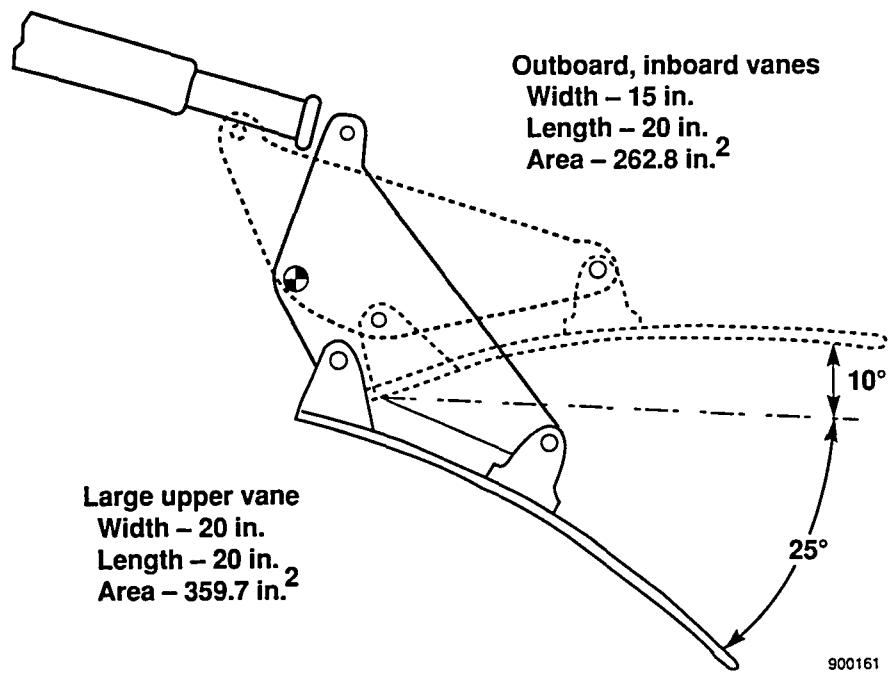
Figure 5. The F/A-18 high alpha research vehicle vane-size comparison.

910851
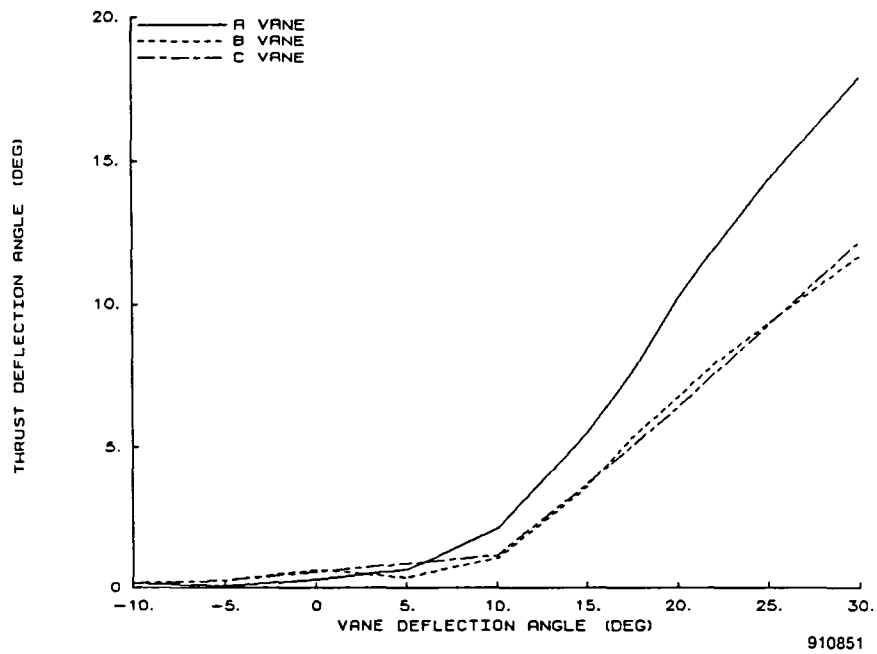
Figure 6. Single-vane deflections at maximum afterburner and nozzle pressure ratio = 2.
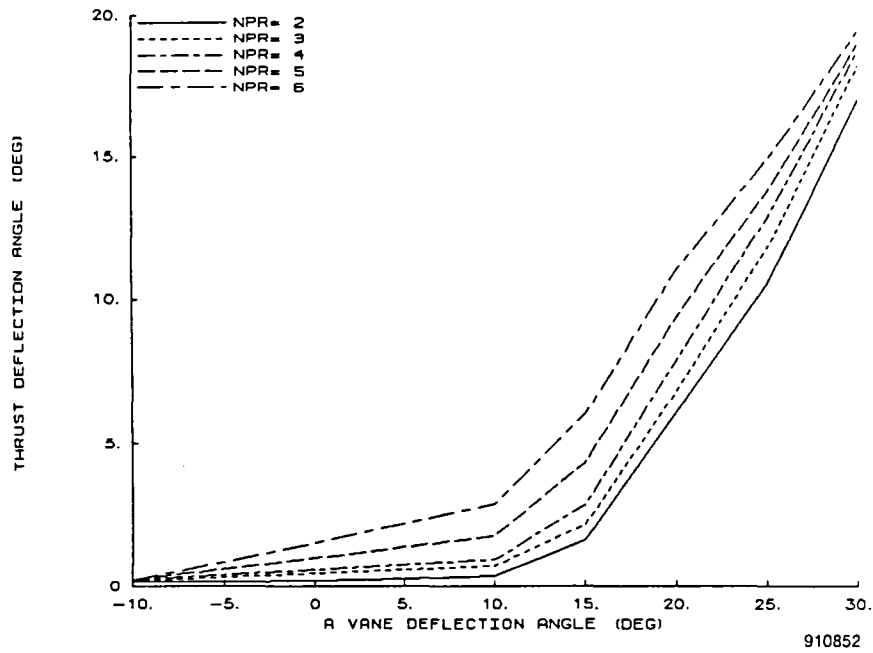
Figure 7. Large vane deflection at military power for various nozzle pressure ratios.
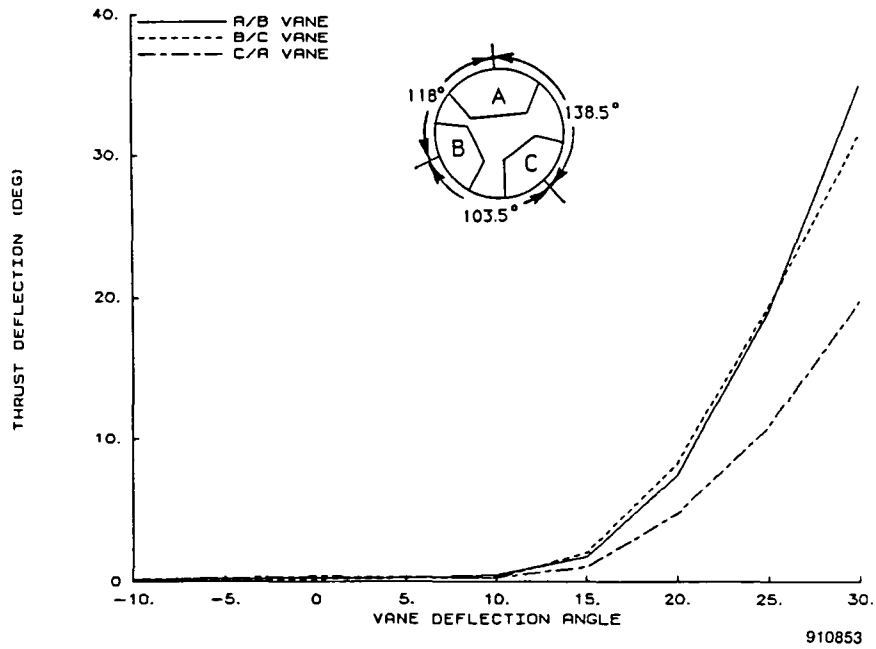
Figure 8. Simultaneous vane deflections at military power and nozzle pressure ratio = 2.

38
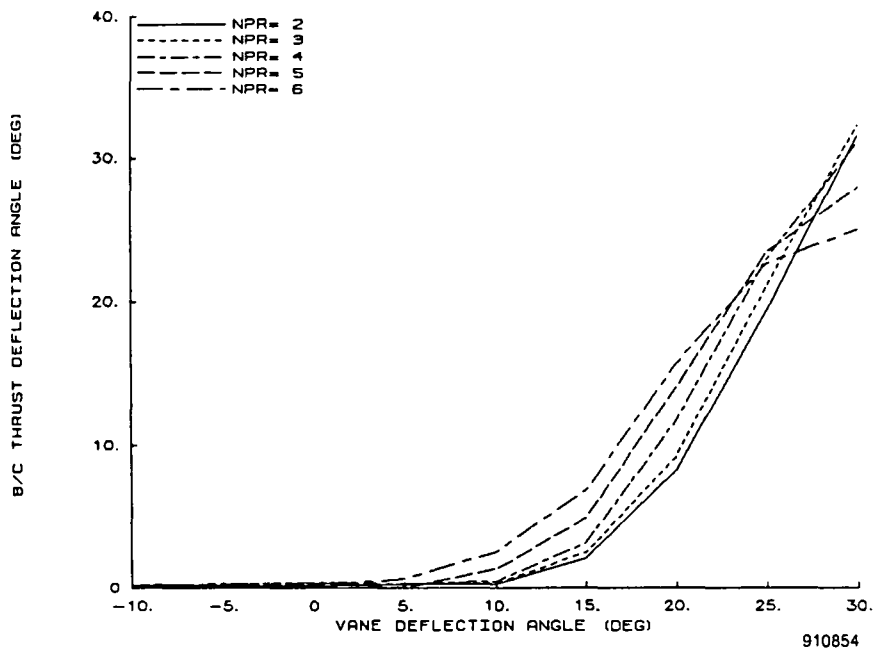
Figure 9. Simultaneous B and C vane deflections at military power for various nozzle pressure ratios.
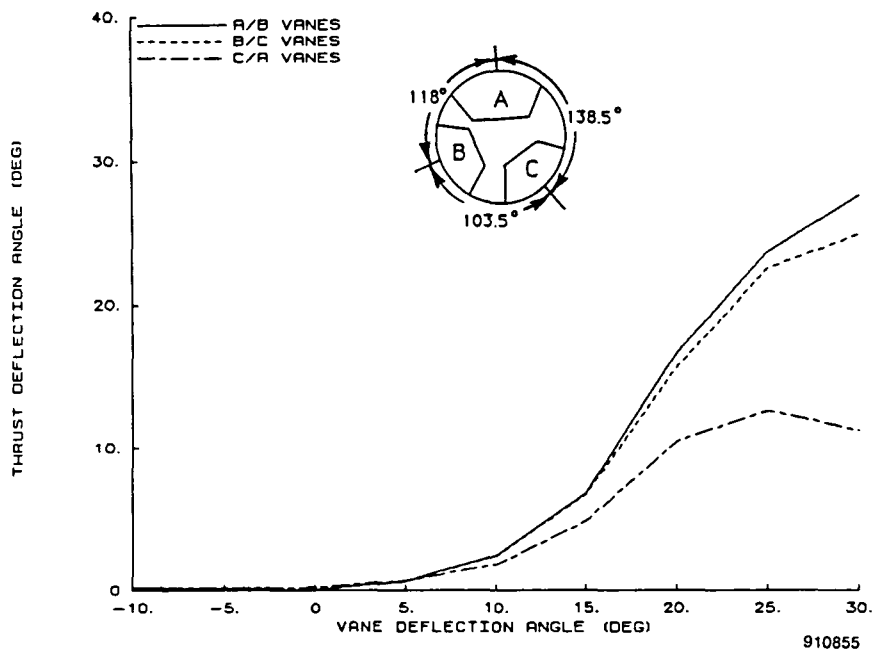
Figure 10. Simultaneous two-vane deflections at military power and nozzle pressure ratio = 6.
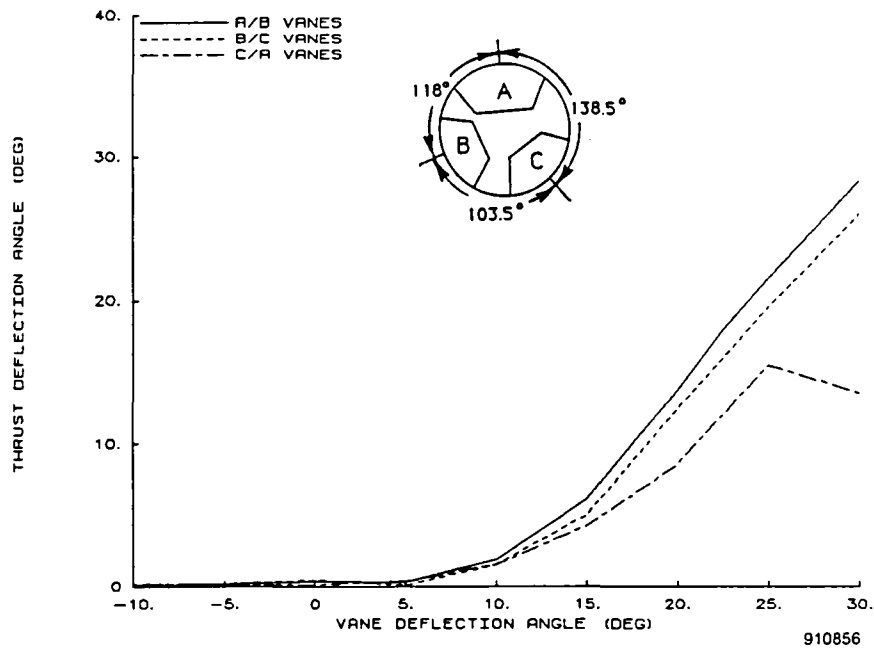
Figure 11. Simultaneous two-vane deflections at maximum afterburner and nozzle pressure ratio = 2.
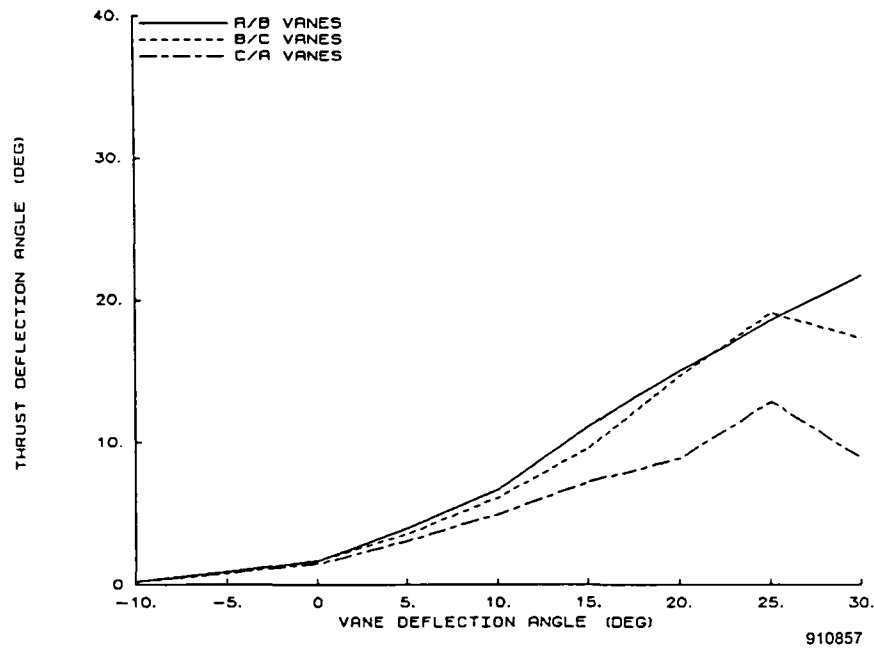
Figure 12. Simultaneous two-vane deflections at maximum afterburner and nozzle pressure ratio = 6.

40
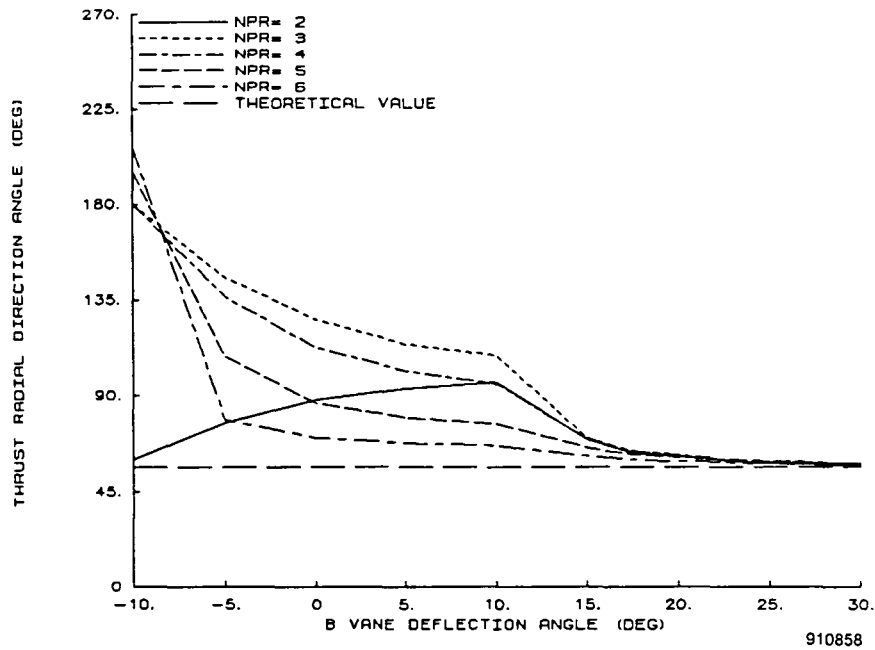
Figure 13. Thrust direction at military power for various nozzle pressure ratios.
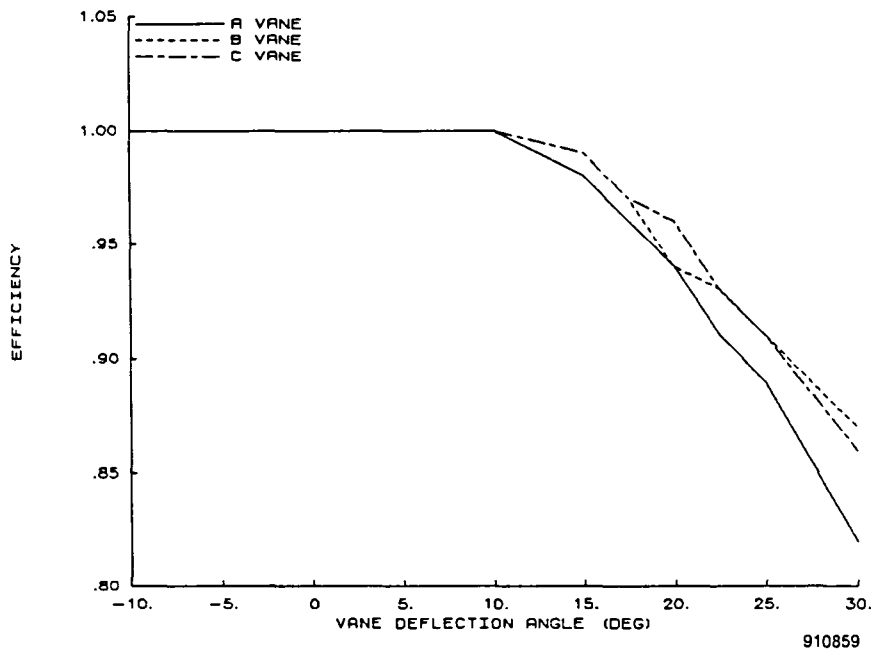
Figure 14. Single-vane efficiencies at military power and nozzle pressure ratio = 2.

41
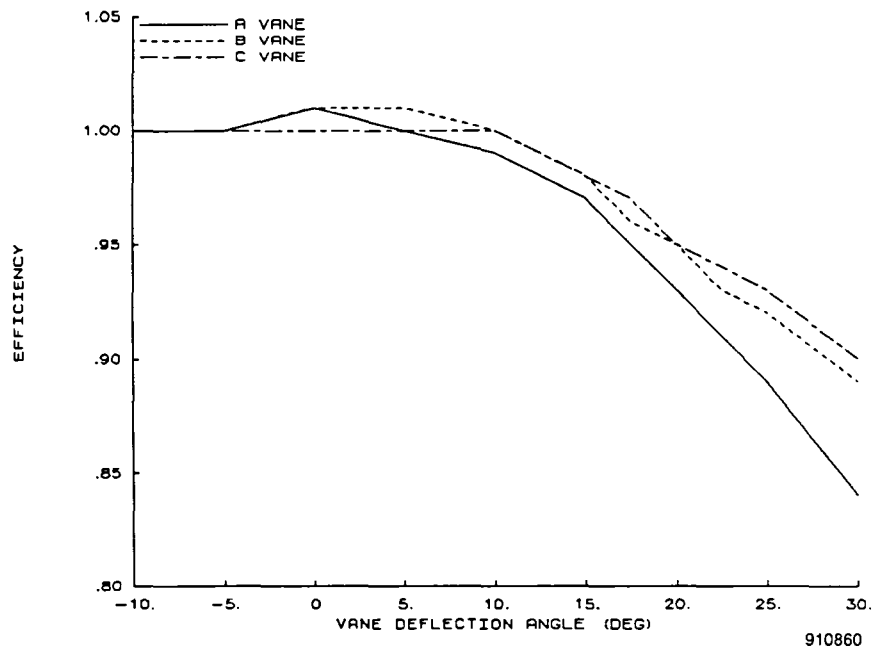
Figure 15. Single-vane efficiencies at maximum afterburner and nozzle pressure ratio = 2.
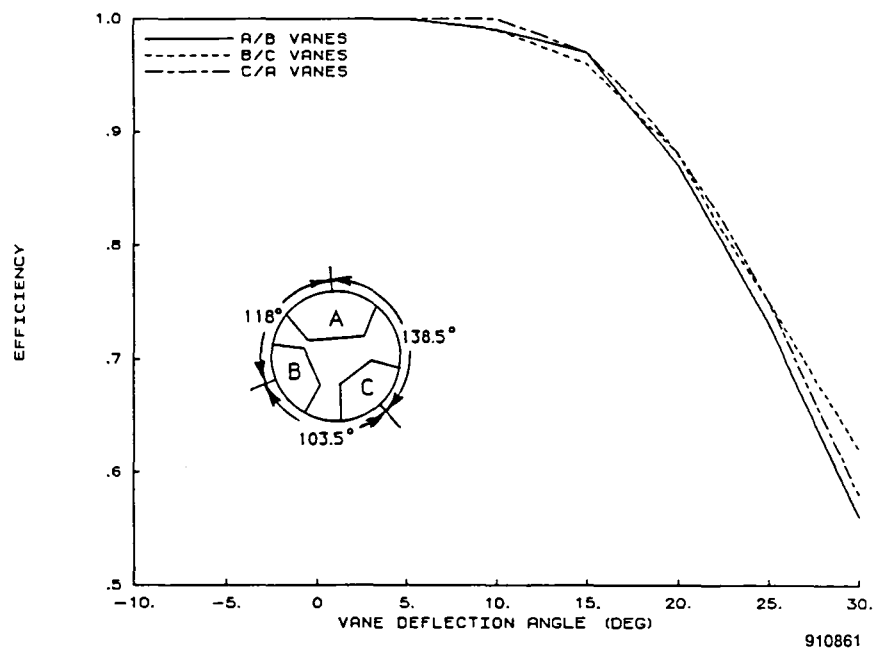
Figure 16. Efficiencies for simultaneous two-vane deflections at military power and nozzle pressure ratio = 2.

42
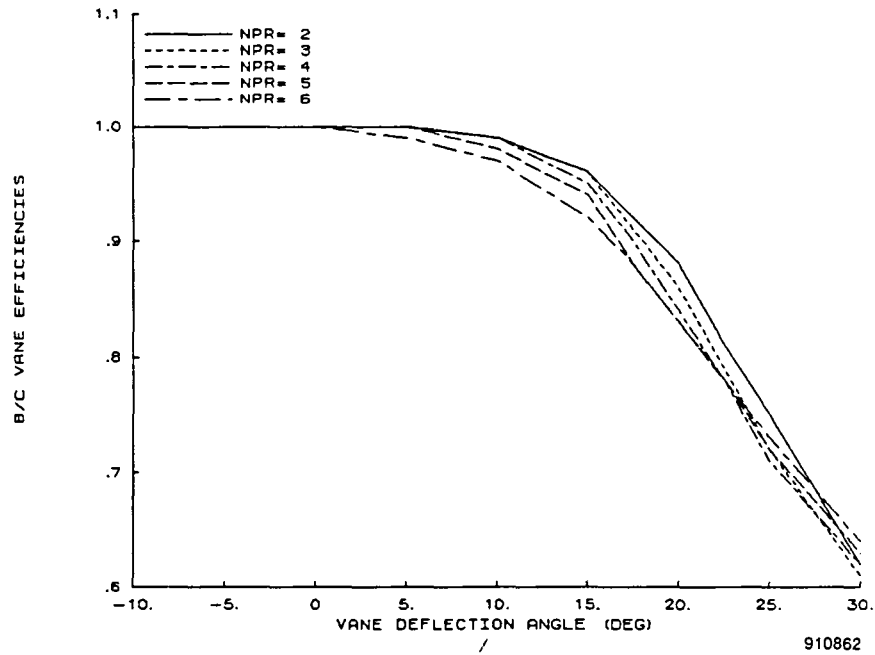
Figure 17. Efficiencies for simultaneous two-vane deflections, at military power, and for various nozzle pressure ratios.

Configuration	Vertical tail height, percent		
A	100		
B	75		
C	50		
D	0		
E	0	No ventral fins	
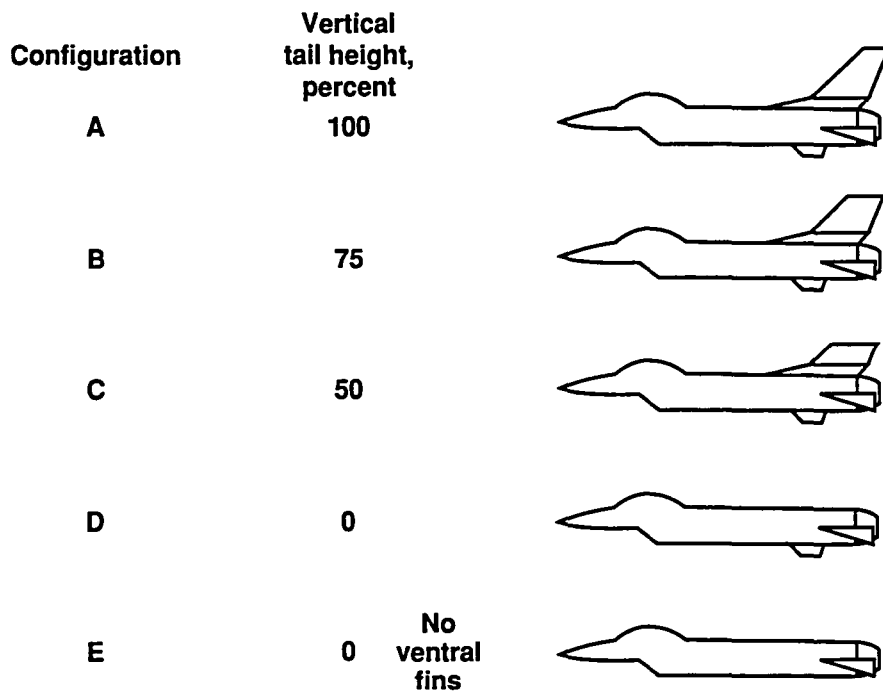
Figure 18. Aerodynamic Preliminary Analysis System II configurations of the F-16 Fighting Falcon.

43
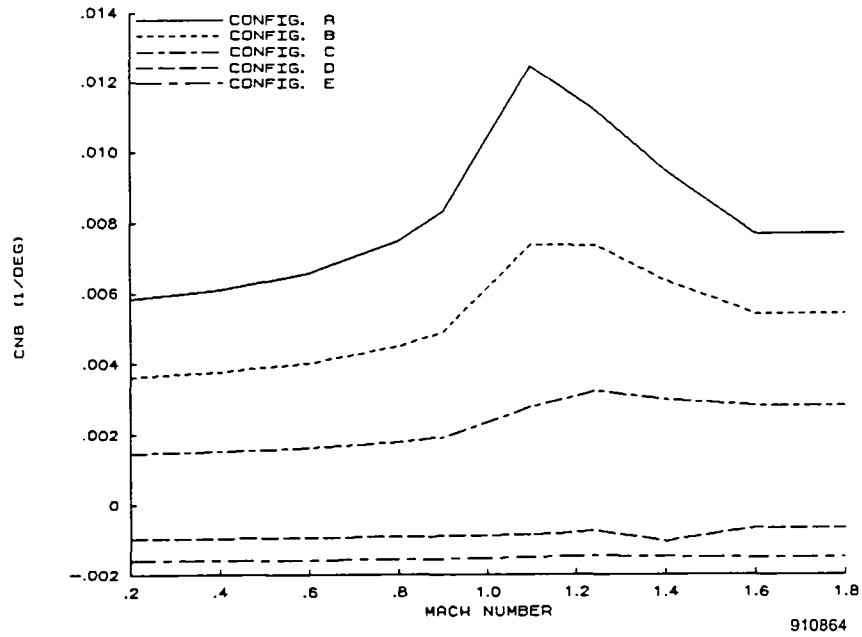
Figure 19. Variation of yawing moment coefficient with sideslip angle.
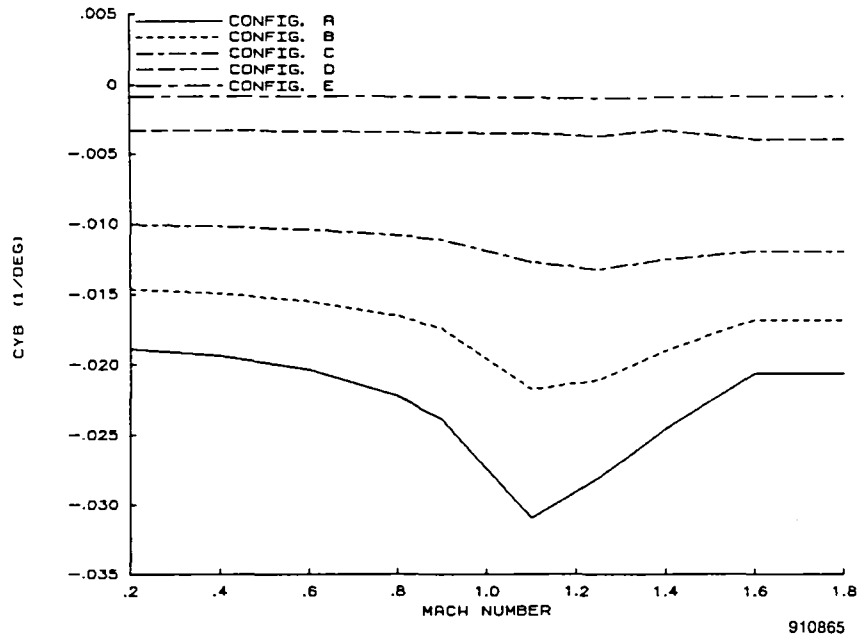
Figure 20. Variation of side force coefficient with sideslip angle.

44
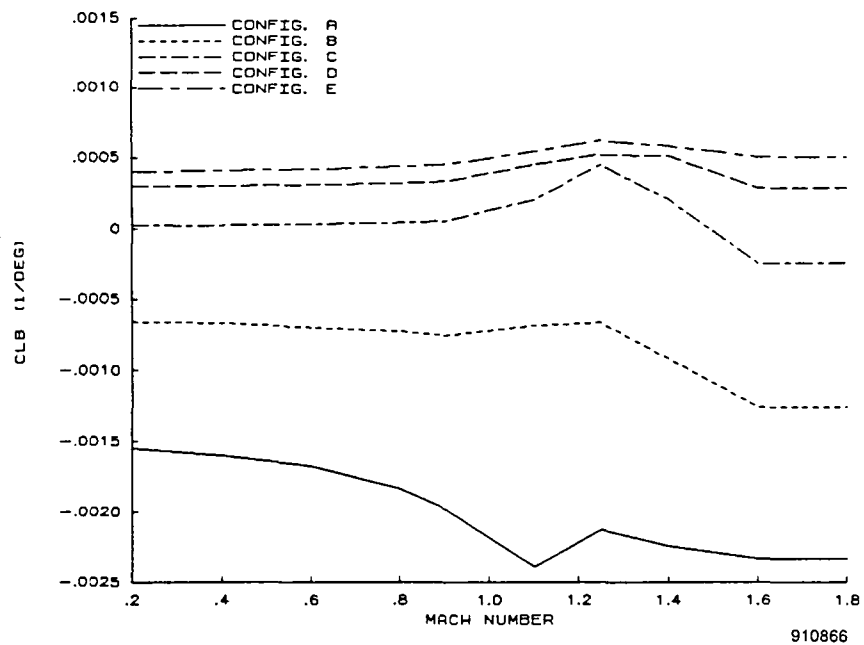
Figure 21. Variation of rolling moment coefficient with sideslip angle.
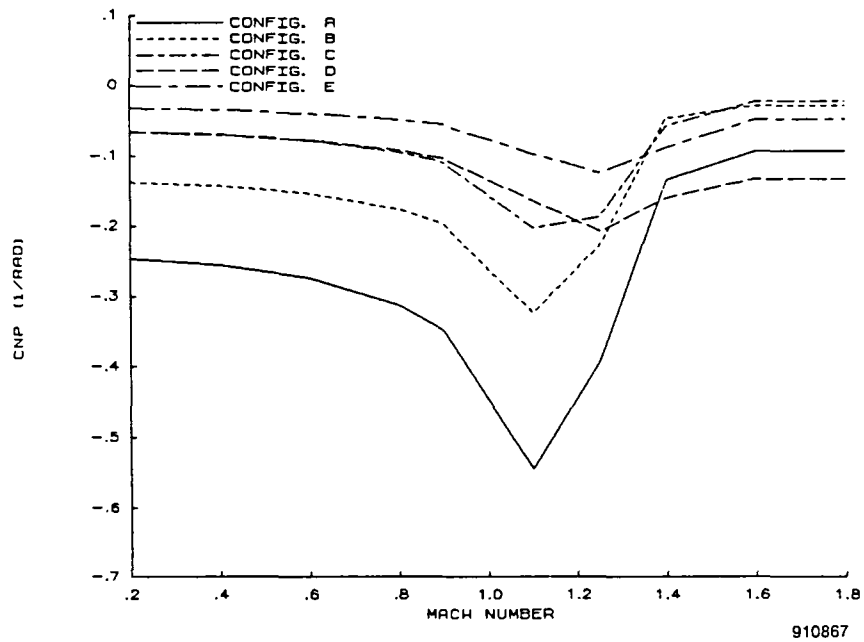
Figure 22. Variation of yawing moment coefficient with roll rate.

45
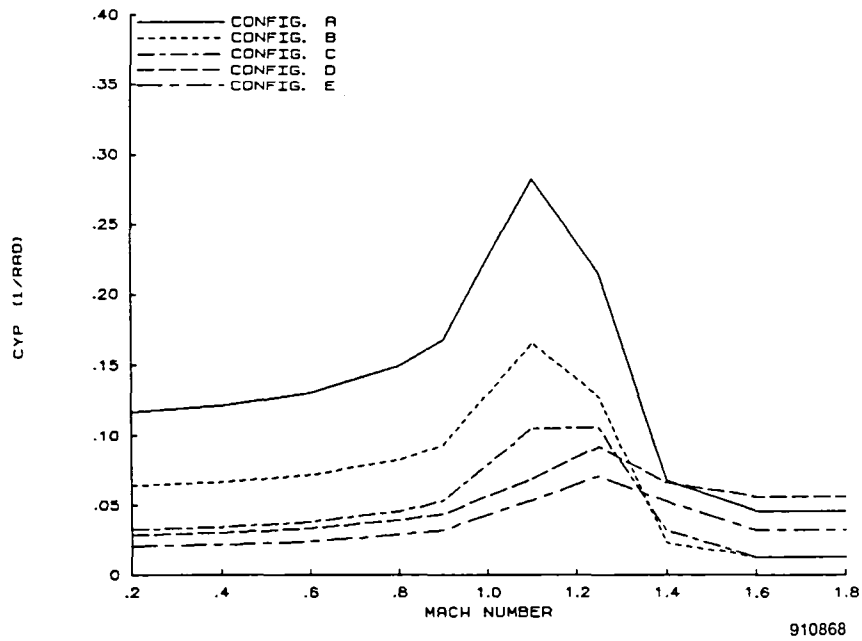
Figure 23. Variation of side force coefficient with roll rate.
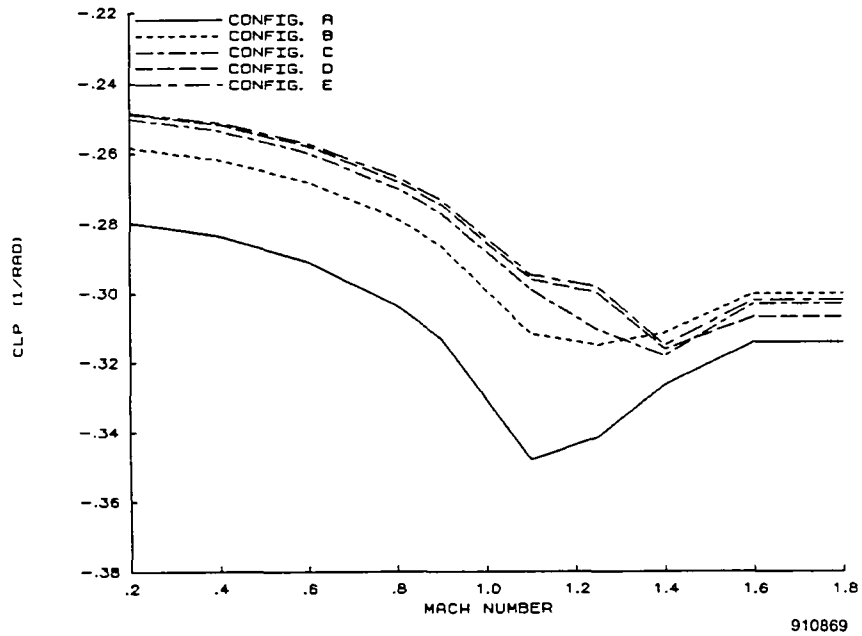
Figure 24. Variation of rolling moment coefficient with roll rate.

46
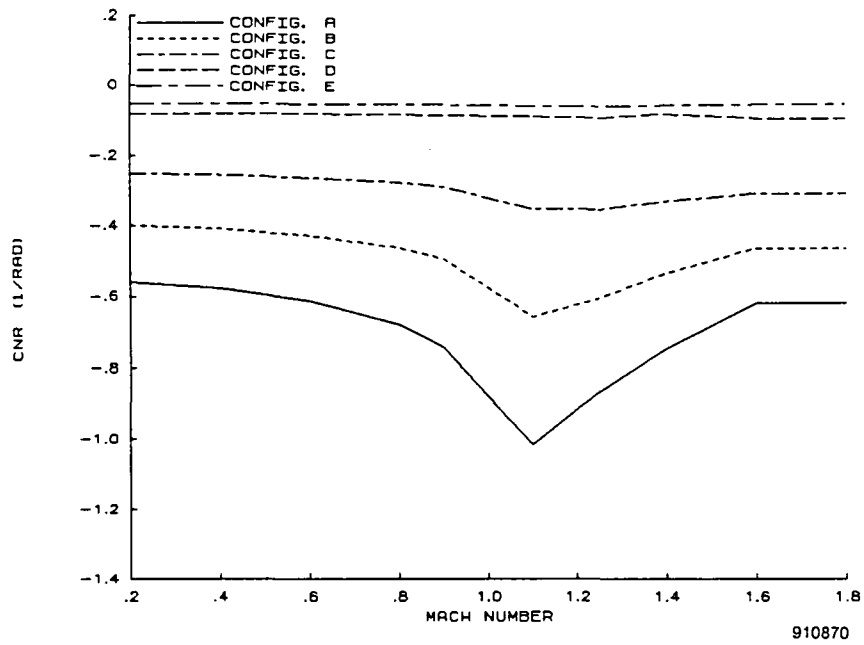
Figure 25. Variation of yawing moment coefficient with yaw rate.
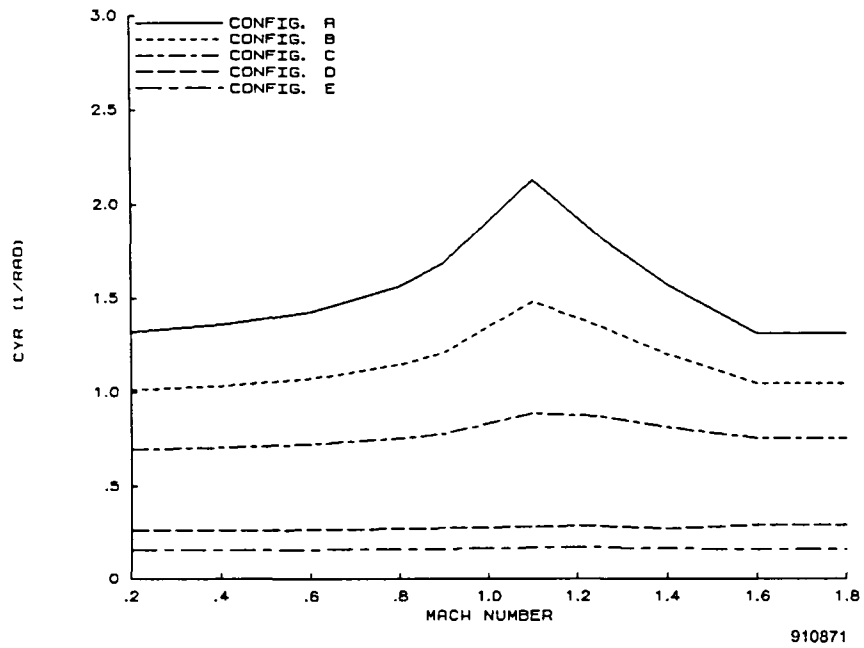
Figure 26. Variation of side force coefficient with yaw rate.

47
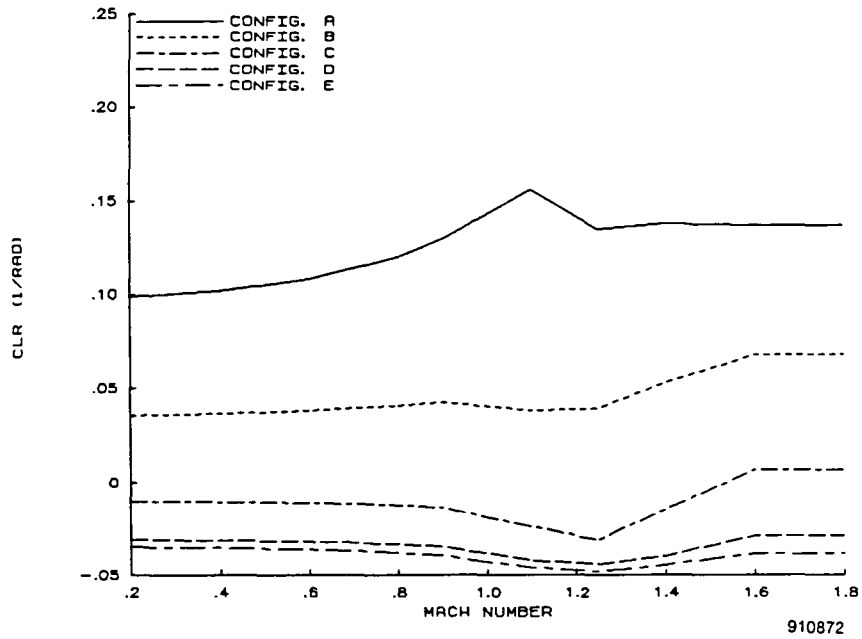
Figure 27. Variation of rolling moment coefficient with yaw rate.
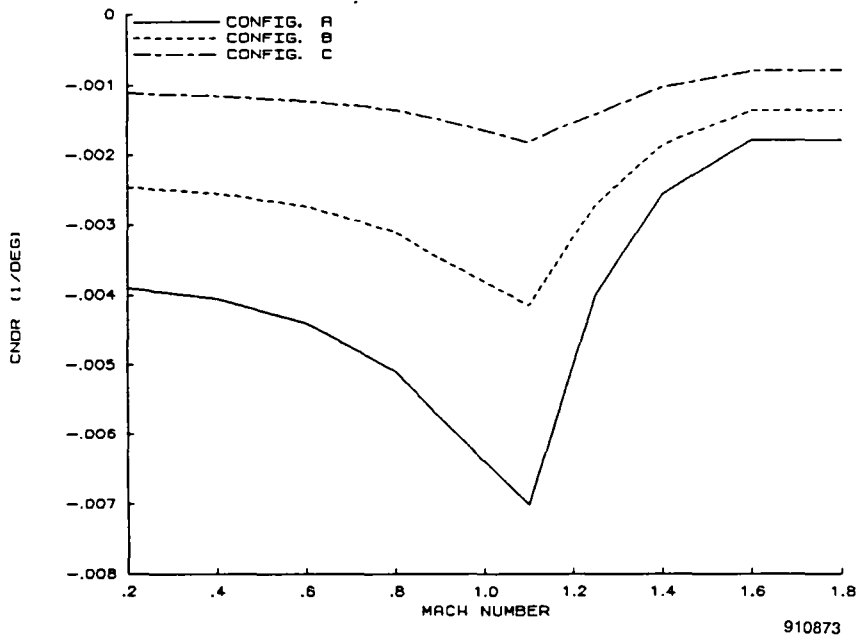
Figure 28. Variation of yawing moment coefficient with rudder deflection.

48
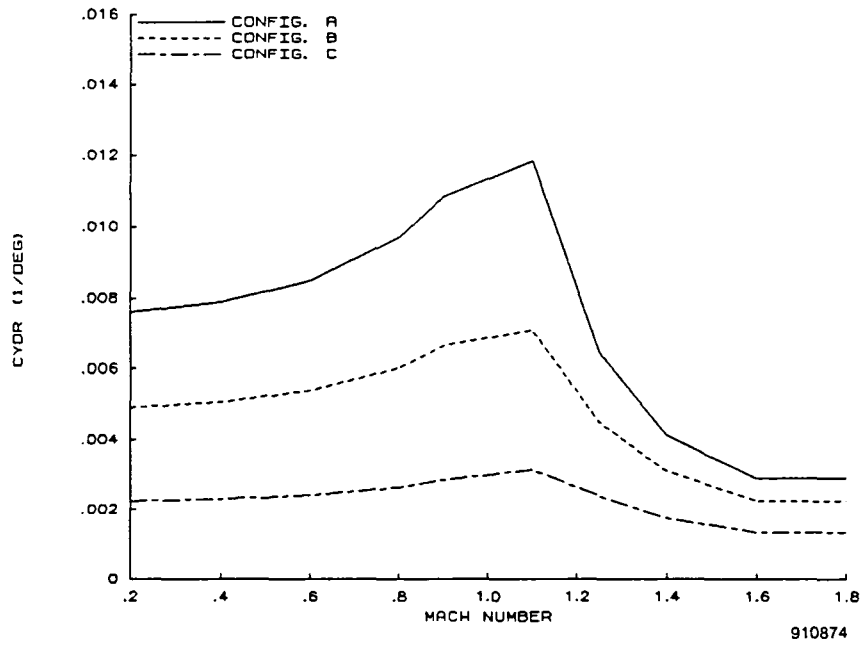
Figure 29. Variation of side force coefficient with rudder deflection.
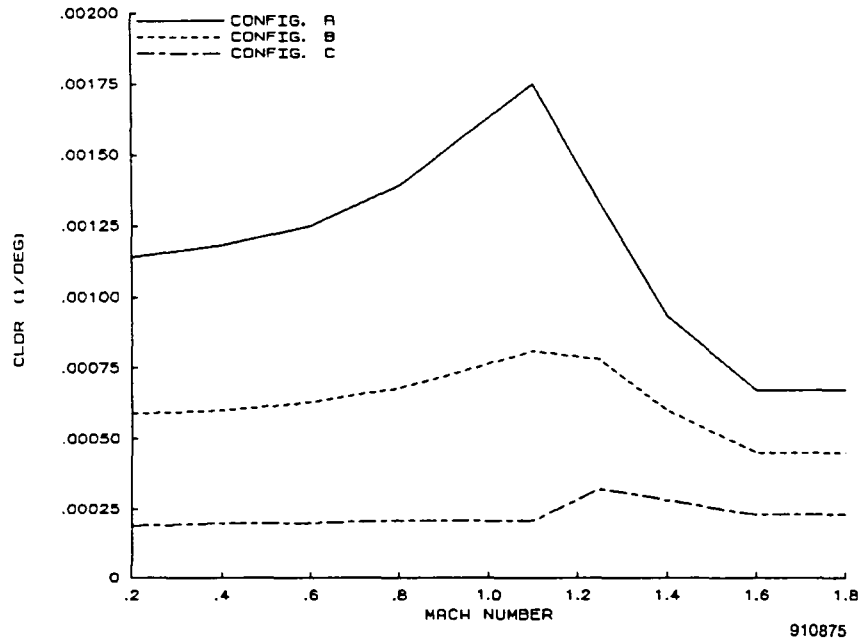
Figure 30. Variation of rolling moment coefficient with rudder deflection.

49
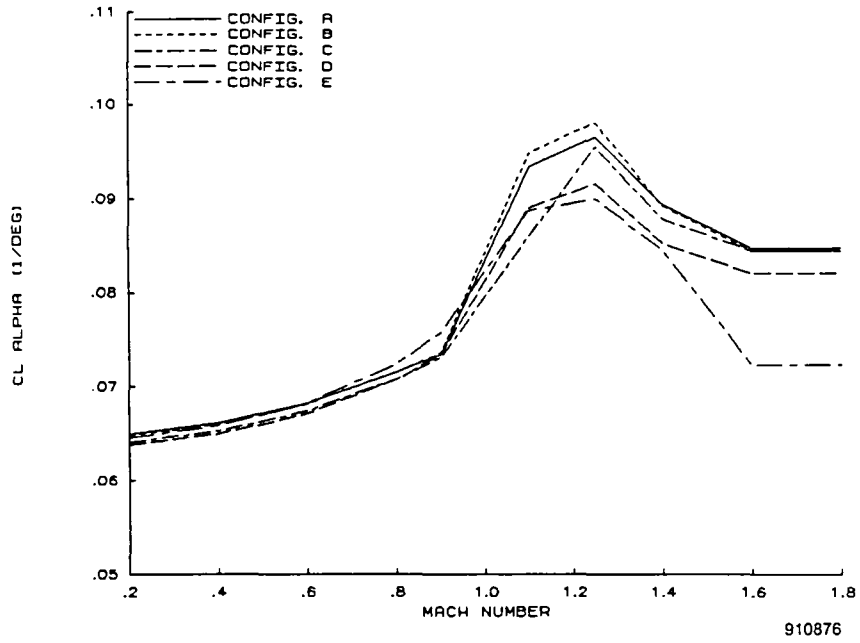
Figure 31. Variation of lift coefficient with angle of attack.
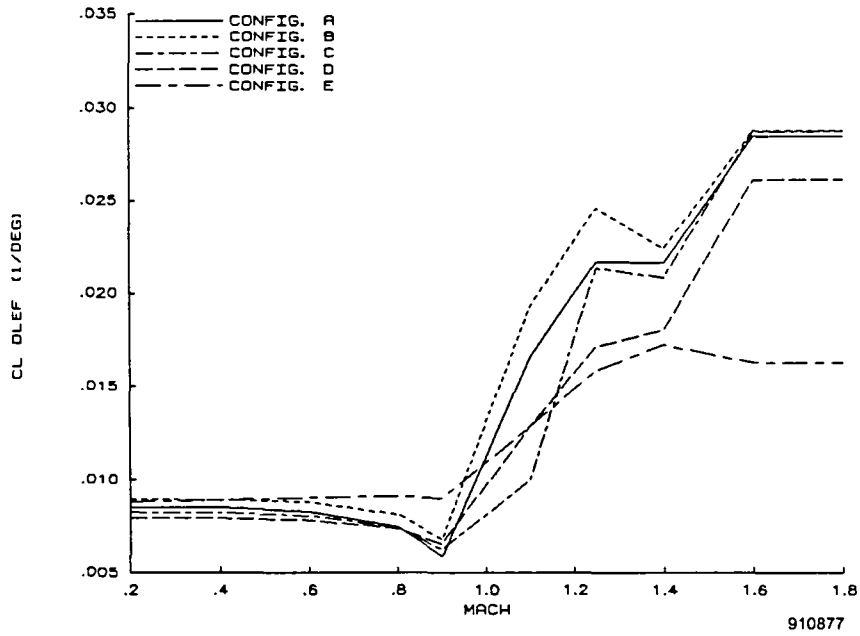
Figure 32. Variation of lift coefficient with leading-edge flap deflection angle.

50
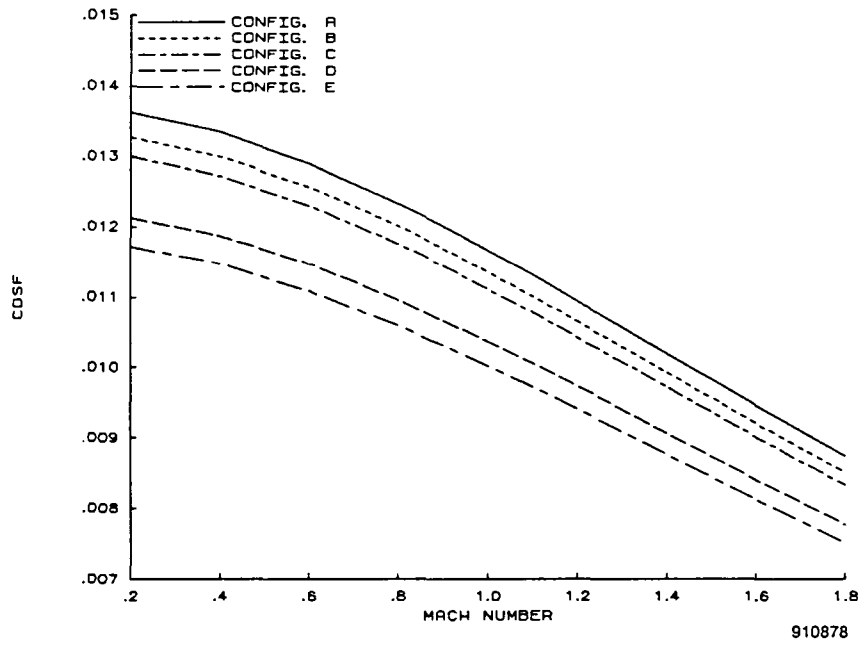
Figure 33. Skin friction drag coefficient.
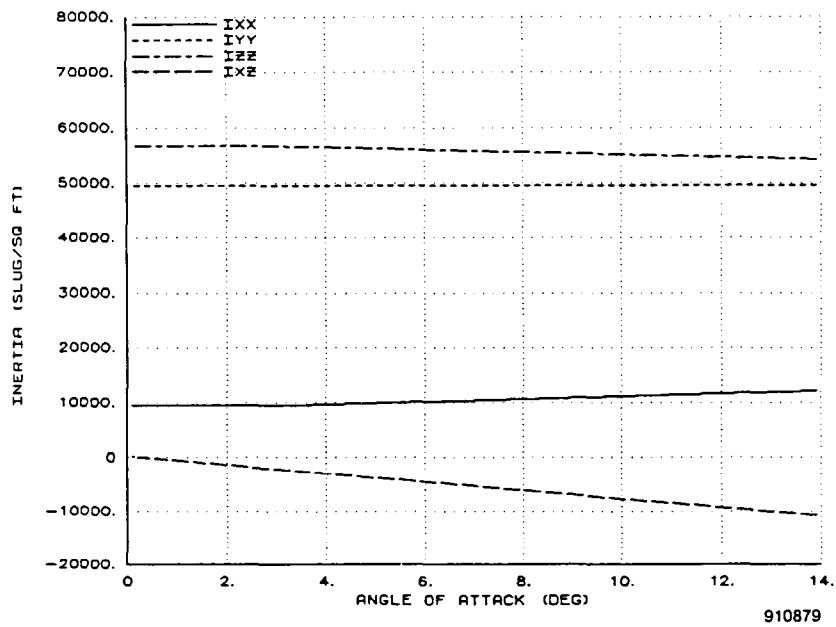
Figure 34. Effects of angle of attack on aircraft inertias.

51
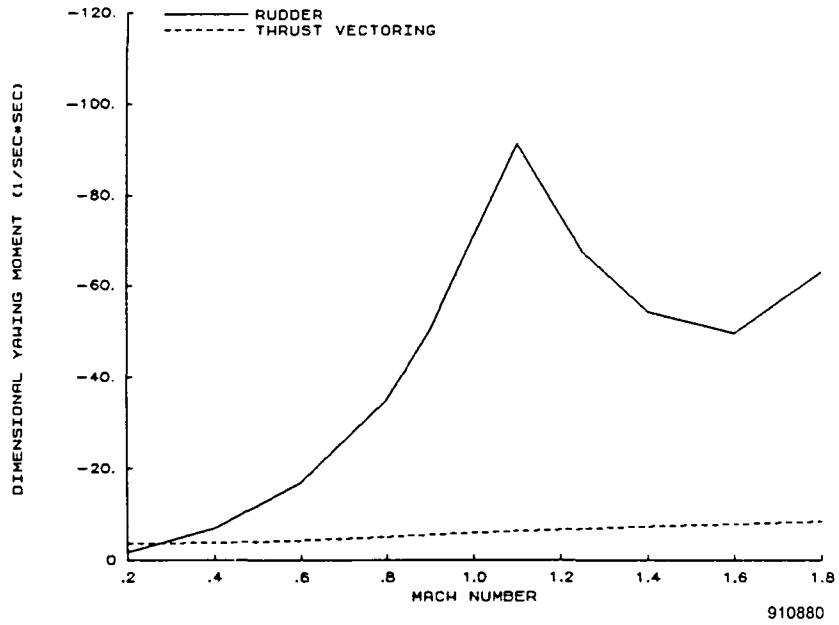
Figure 35. Dimensional yawing moments caused by the rudder and thrust vectoring control system at maximum afterburner and sea level.
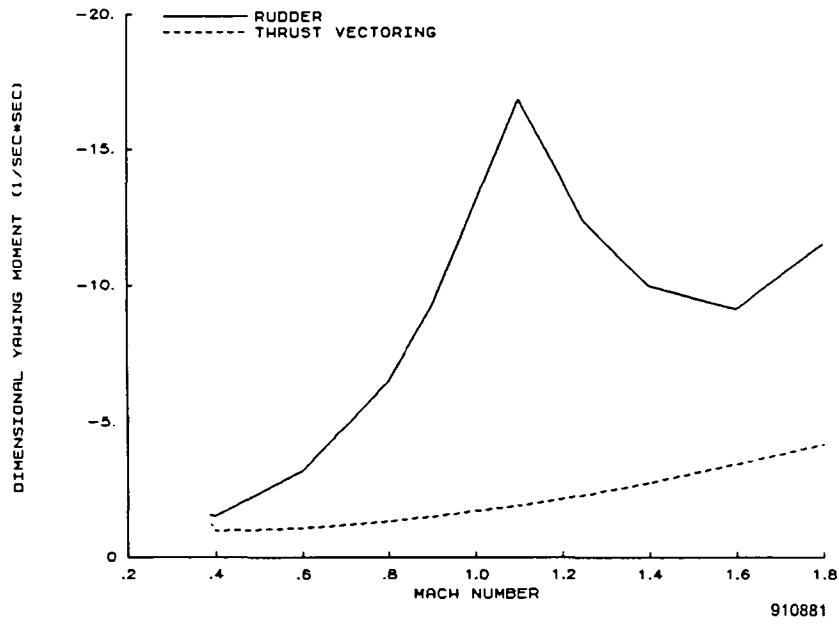
Figure 36. Dimensional yawing moments caused by the rudder and thrust vectoring control system at maximum afterburner and 40,000 ft.

52
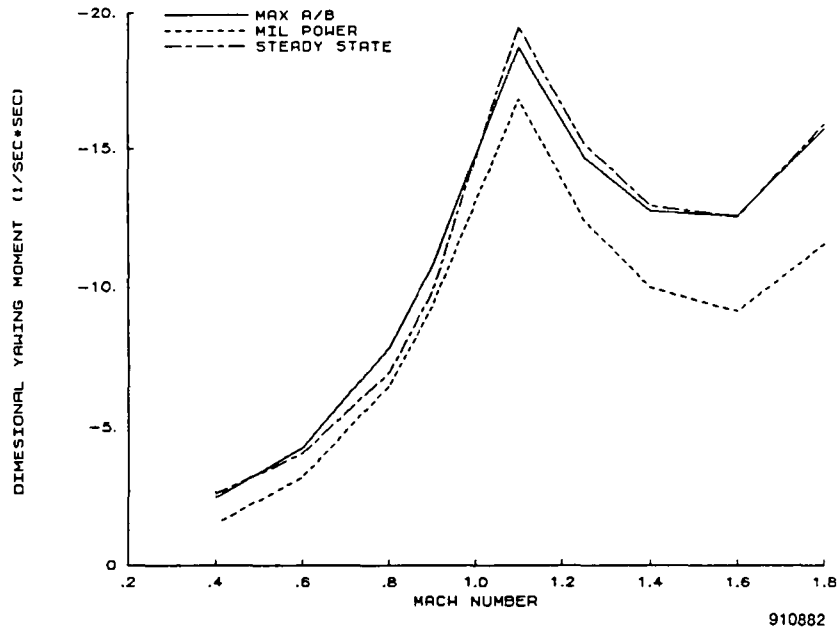
Figure 37. Total yawing moment control for various engine thrust settings for configuration A.
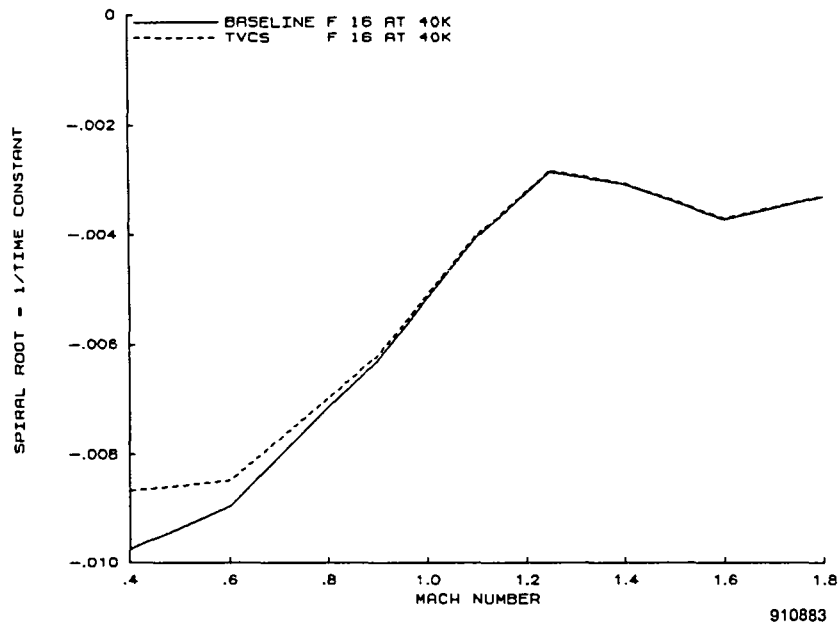
Figure 38. Spiral mode root changes with thrust vectoring control system addition at 40,000 ft for configuration A.

53
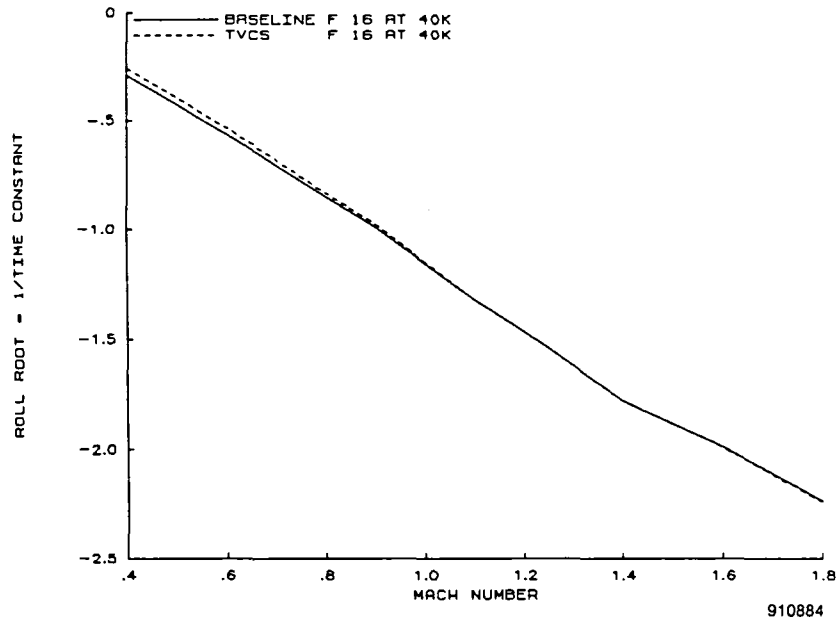
Figure 39. Rolling mode root changes with thrust vectoring control system addition at 40,000 ft for configuration A.
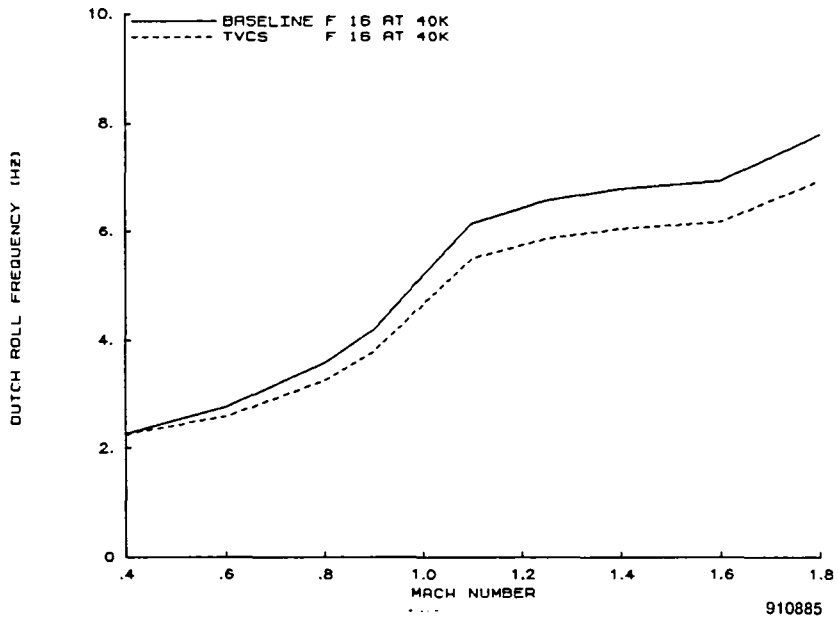
Figure 40. Dutch roll frequency changes with thrust vectoring control system addition at 40,000 ft for configuration A.

54
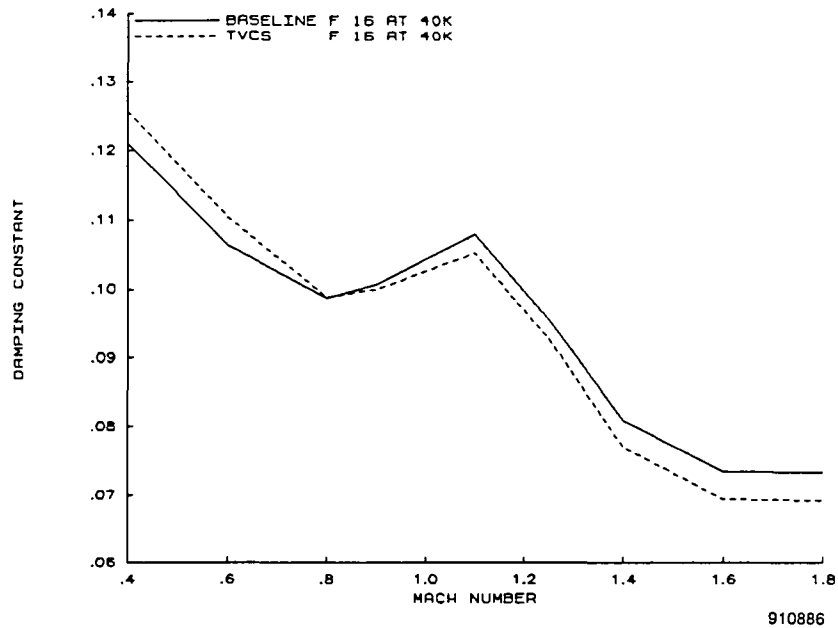
Figure 41. Dutch roll damping changes with thrust vectoring control system addition at 40,000 ft for configuration A.
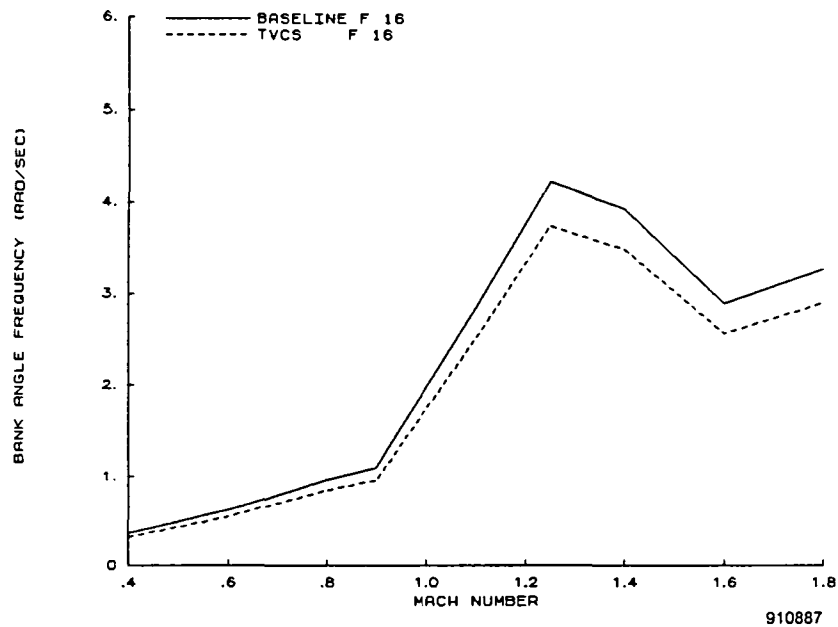
Figure 42. Bank angle frequency changes with thrust vectoring control system addition at 40,000 ft for configuration A.

55
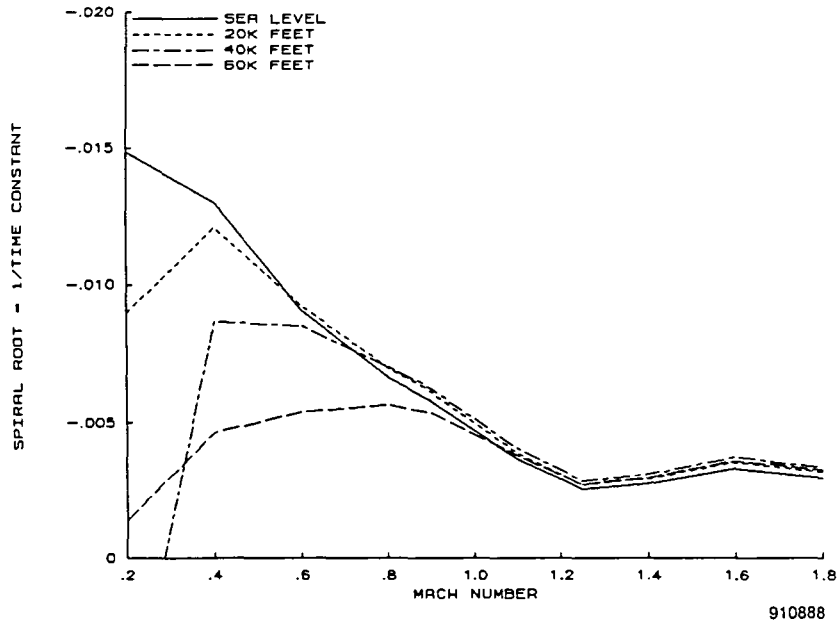
Figure 43. Altitude effects on spiral mode root for configuration A.
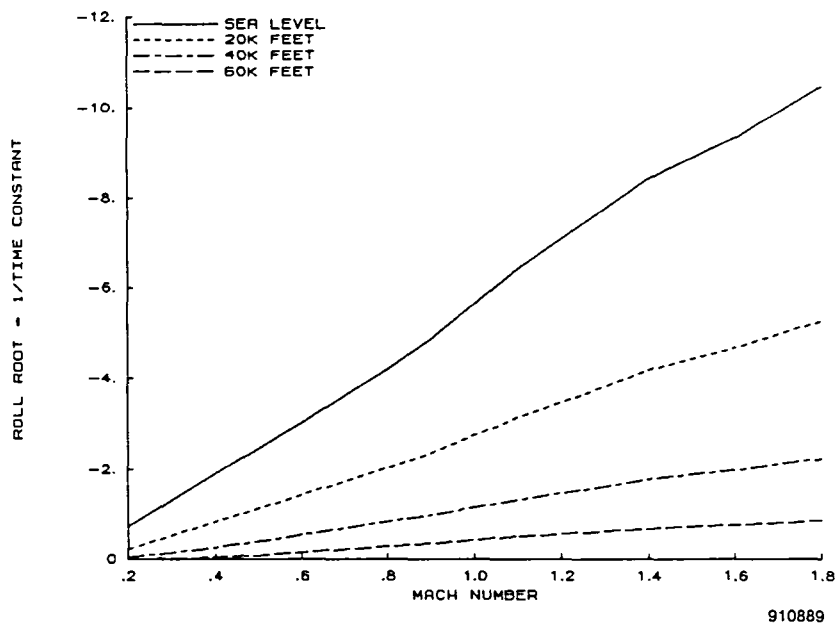
Figure 44. Altitude effects on roll mode root for configuration A.
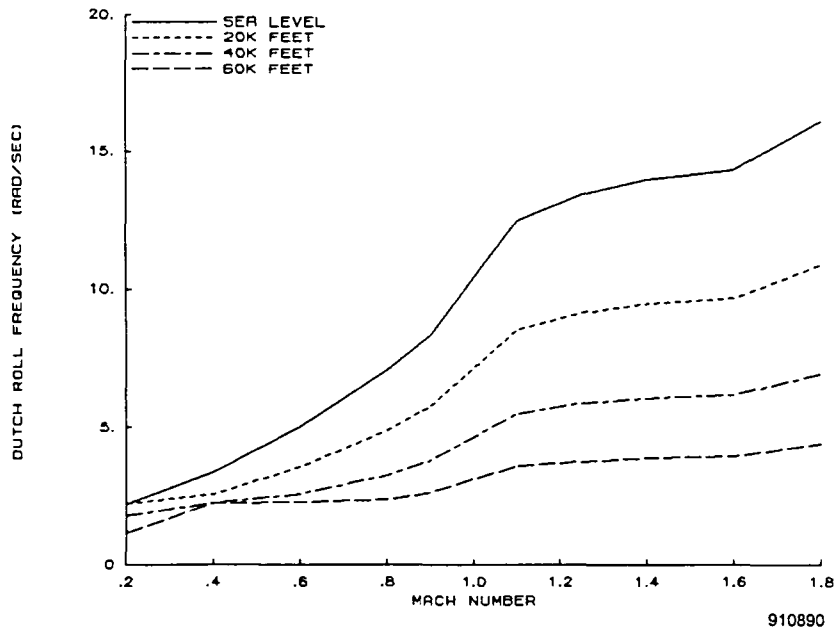
Figure 45. Altitude effects on dutch roll frequency for configuration A.
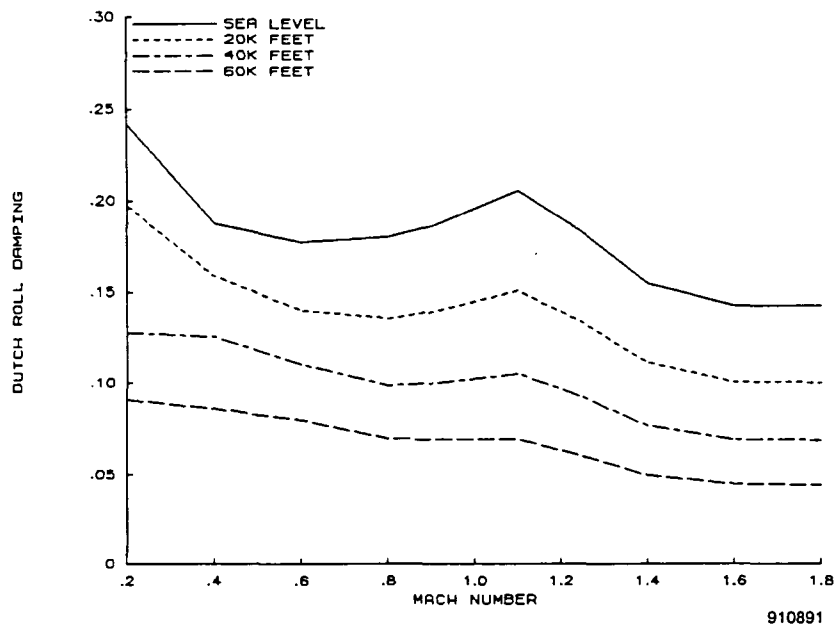
Figure 46. Altitude effects on dutch roll damping for configuration A.
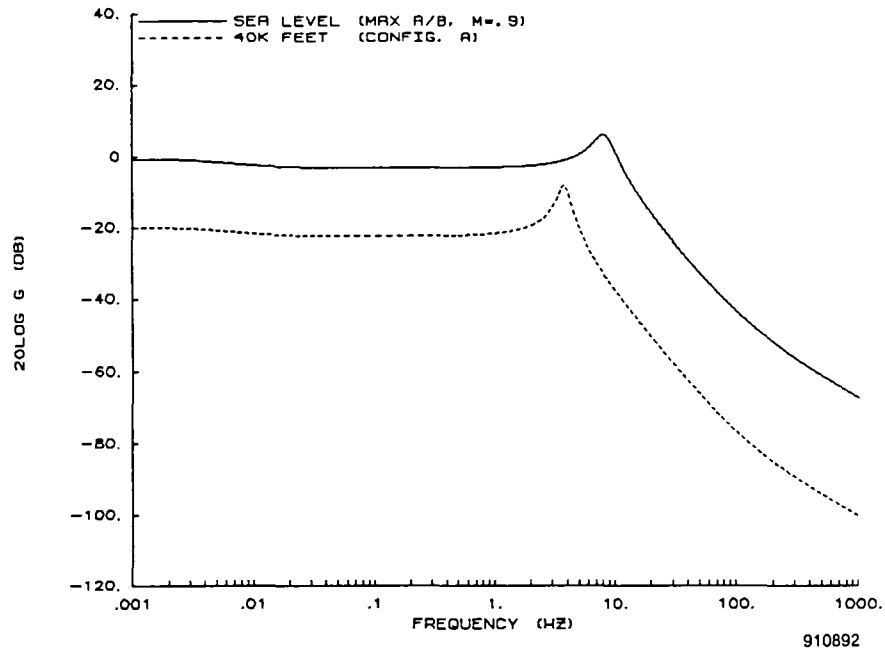
Figure 47. Altitude effects on the sideslip angle magnitude characteristics for configuration A at maximum afterburner and M = 0.9.
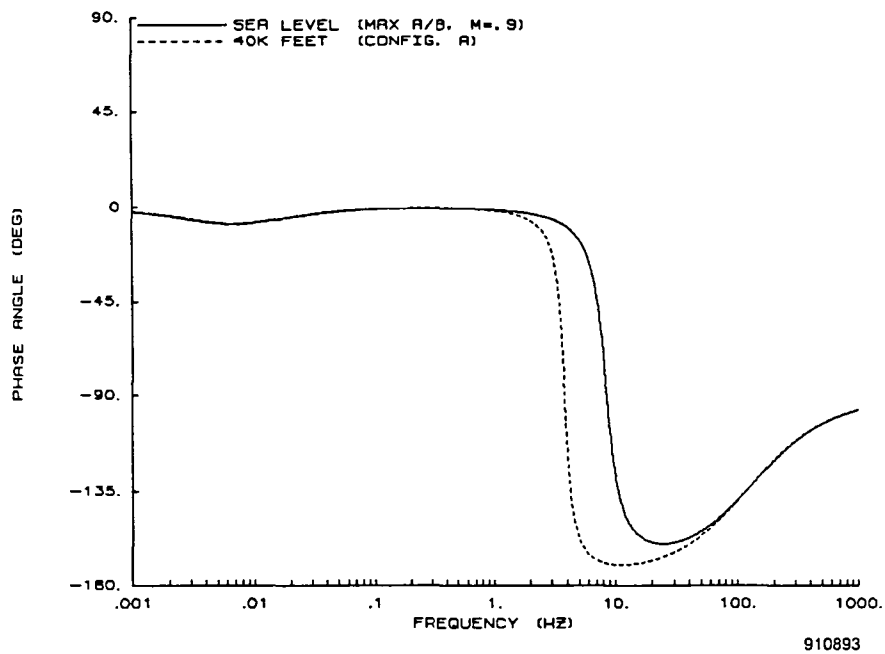
Figure 48. Altitude effects on the sideslip angle phase characteristics for configuration A at maximum afterburner and M = 0.9.

58
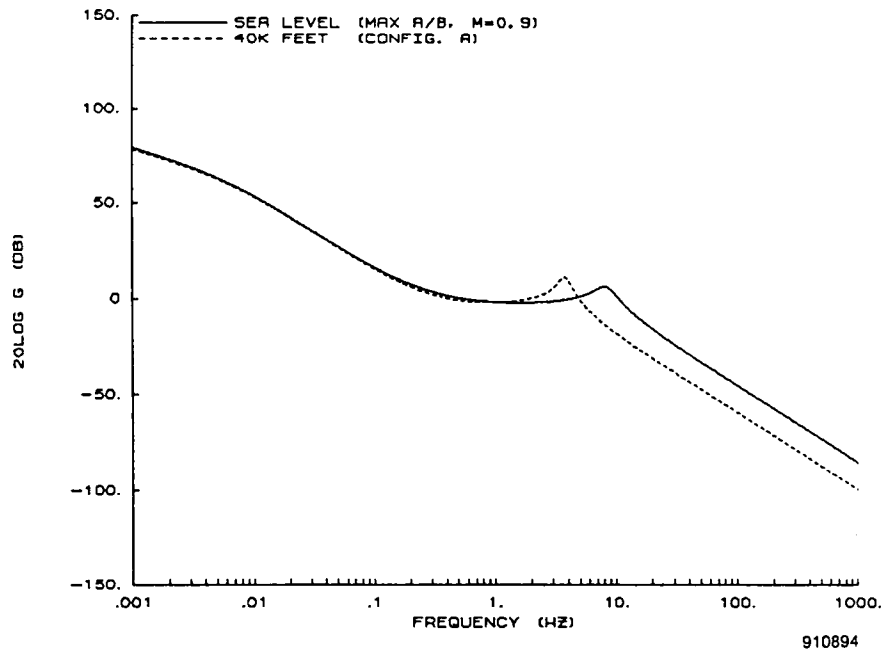
Figure 49. Altitude effects on the heading angle magnitude characteristics for configuration A at maximum afterburner and M = 0.9.
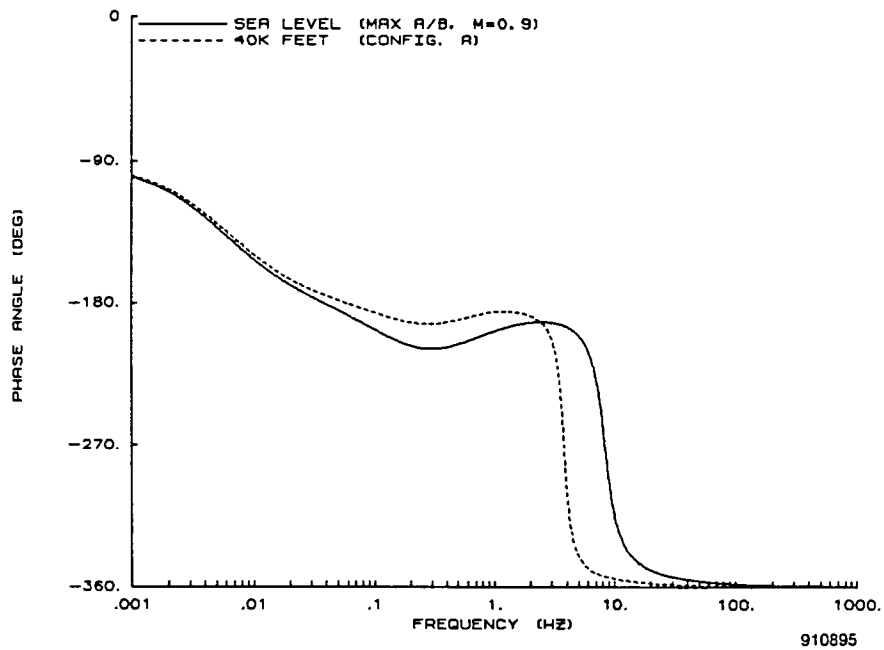
Figure 50. Altitude effects on the heading angle phase characteristics for configuration A at maximum afterburner and M = 09.
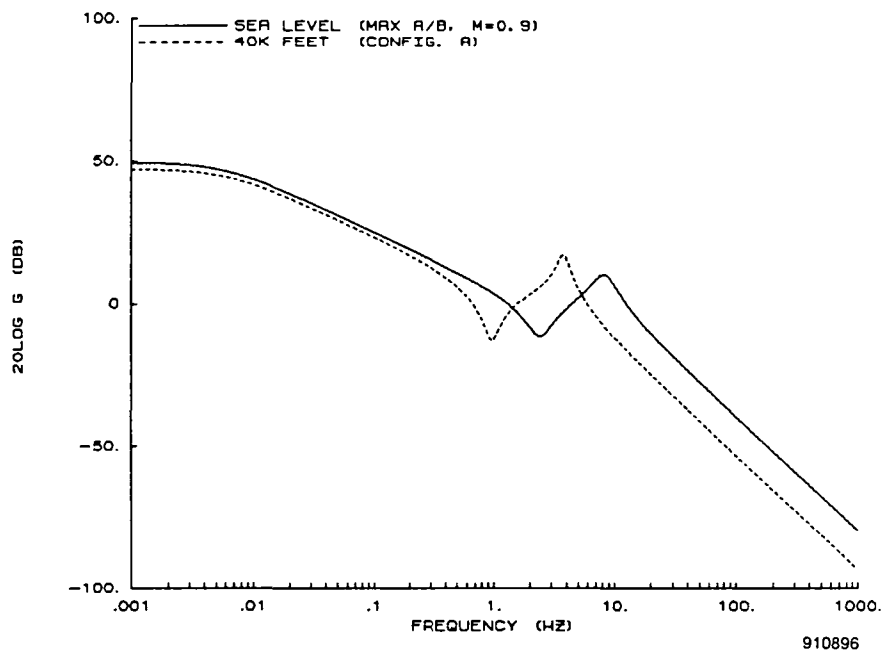
Figure 51. Altitude effects on the roll angle magnitude characteristics for configuration A at maximum afterburner and M = 0.9.
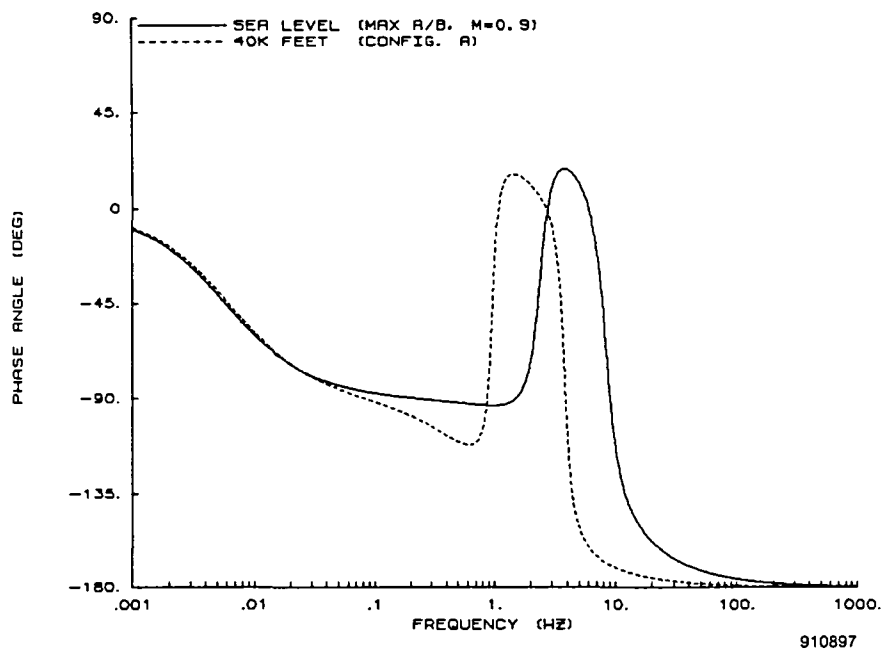
Figure 52. Altitude effects on the roll angle phase characteristics for configuration A at maximum afterburner and M = 0.9.
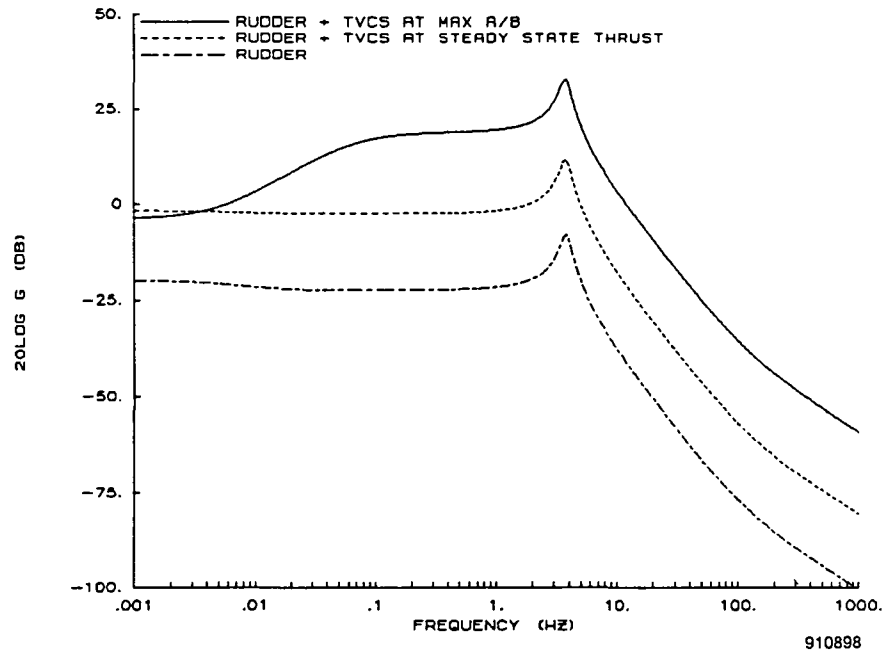
Figure 53. Effects of thrust vectoring control power on sideslip angle magnitude characteristics for various engine settings for configuration A at 40,000 ft and M = 0.9.
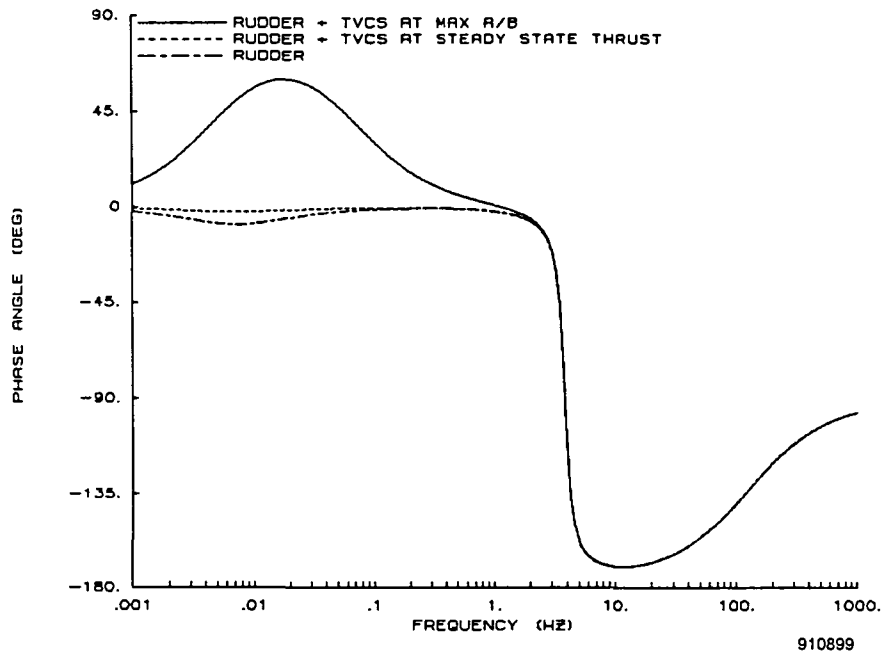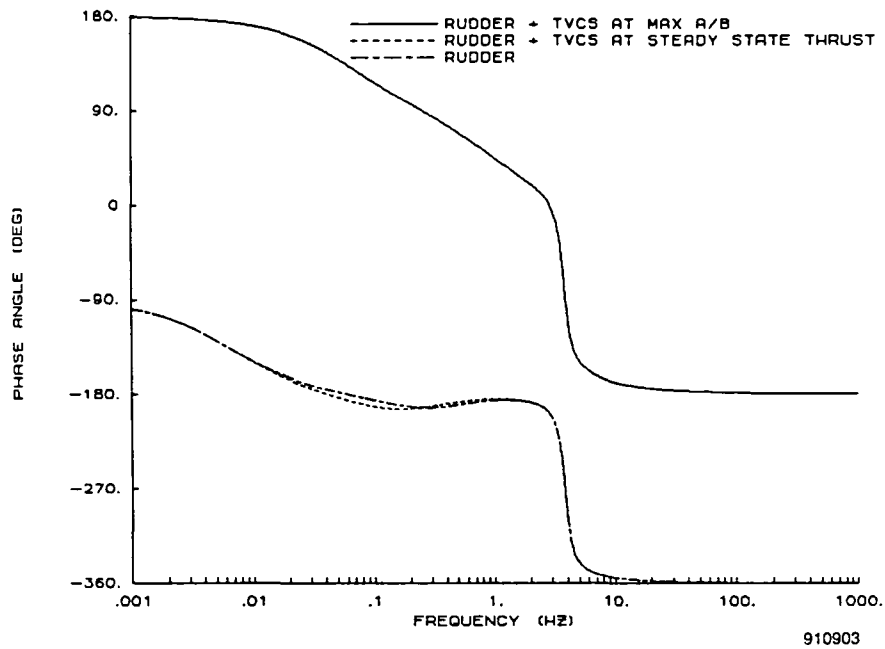

Figure 54. Effects of thrust vectoring control power on sideslip angle phase characteristics for various engine settings for configuration A at 40,000 ft and M = 0.9.
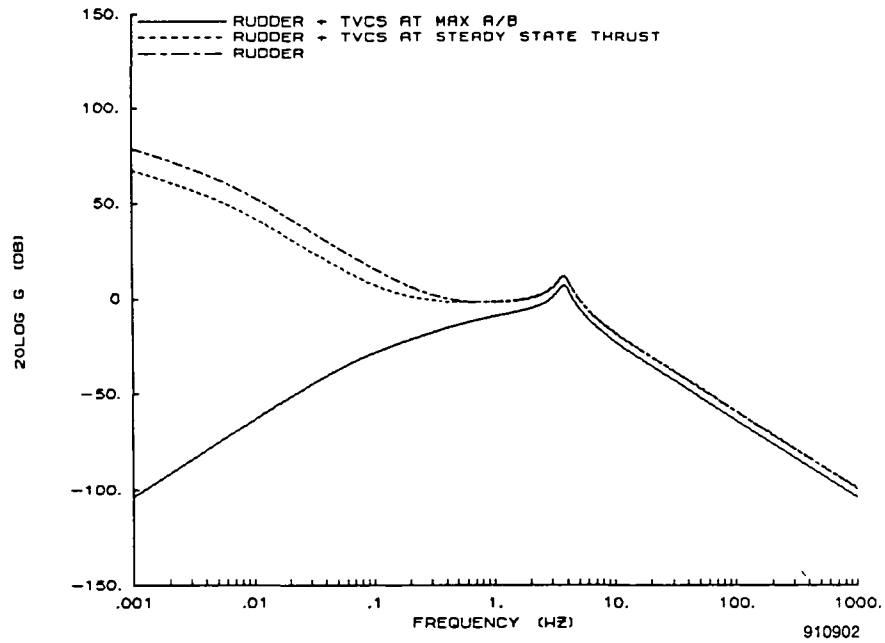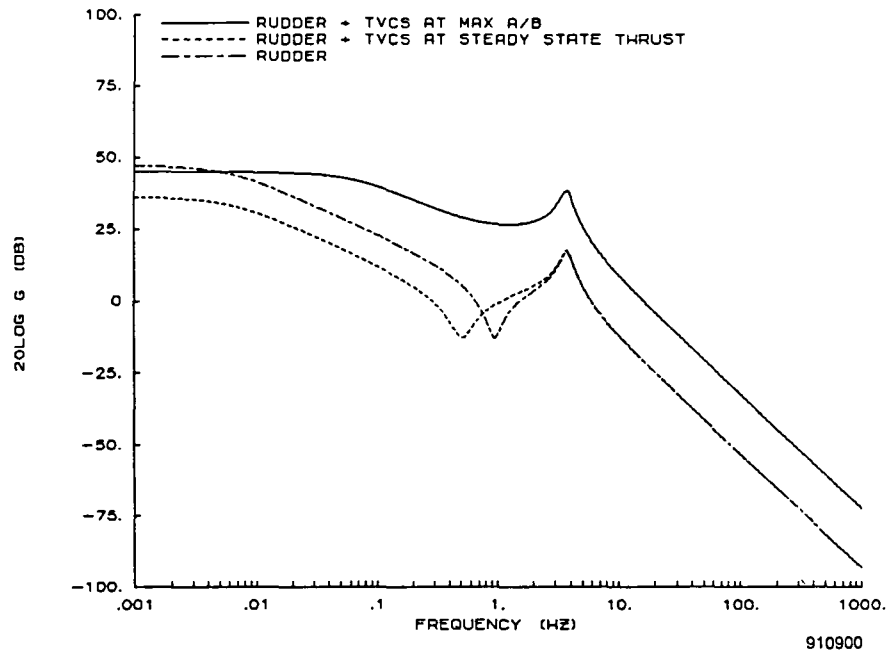
Figure 55. Effects of thrust vectoring control power on heading angle magnitude characteristics for various engine settings for configuration A at 40,000 ft and M = 0.9.
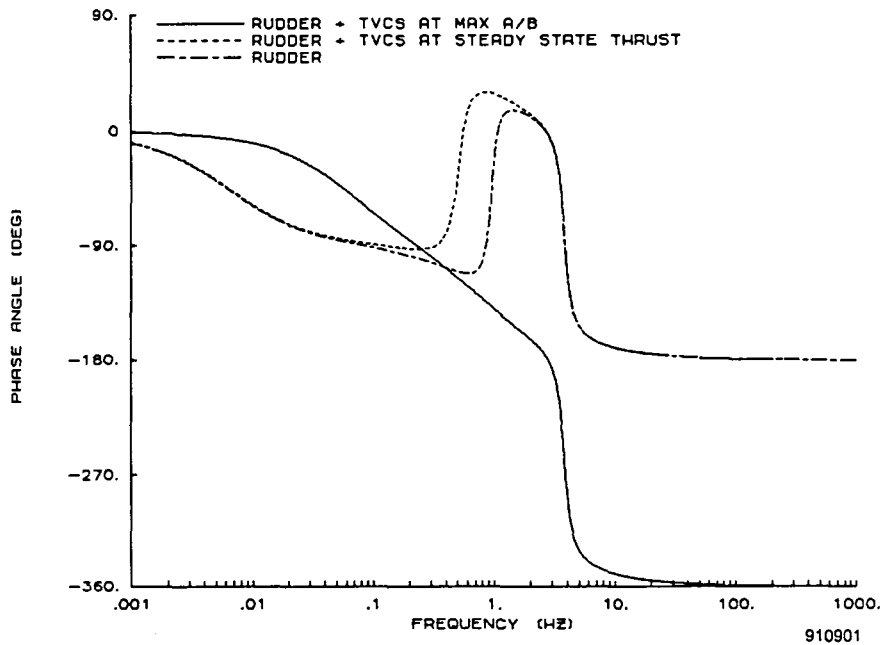

Figure 56. Effects of thrust vectoring control power on heading angle phase characteristics for various engine settings for configuration A at 40,000 ft and M = 0.9.

Figure 57. Effects of thrust vectoring control power on bank angle magnitude characteristics for various engine settings for configuration A at 40,000 ft and M = 0.9.

Figure 58. Effects of thrust vectoring control power on bank angle phase characteristics for various engine settings for configuration A at 40,000 ft and M = 0.9.
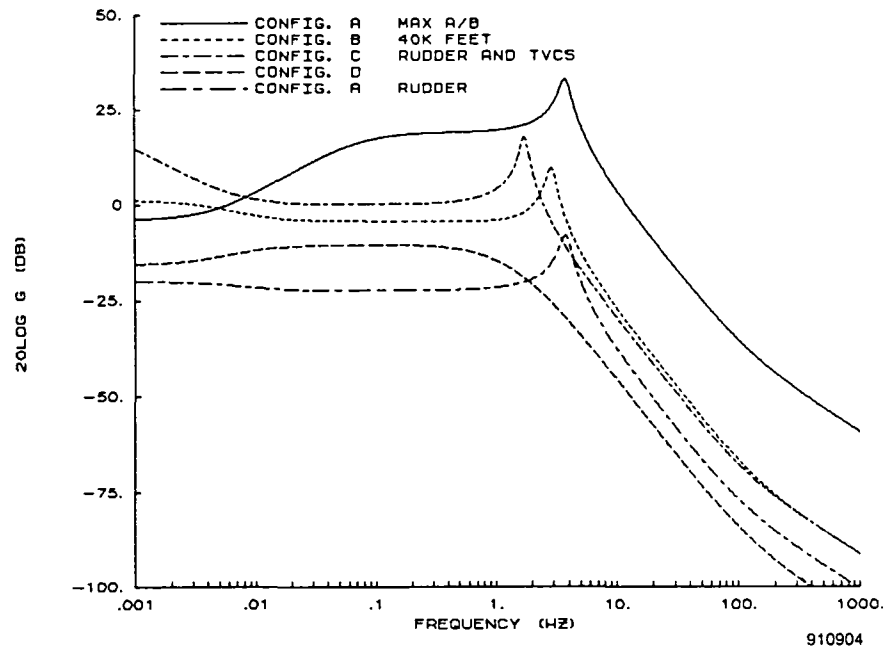
63

Figure 59. Effects of tail size on sideslip angle magnitude characteristics at maximum afterburner, 40,000 ft, and M = 0.9 with thrust vectoring.
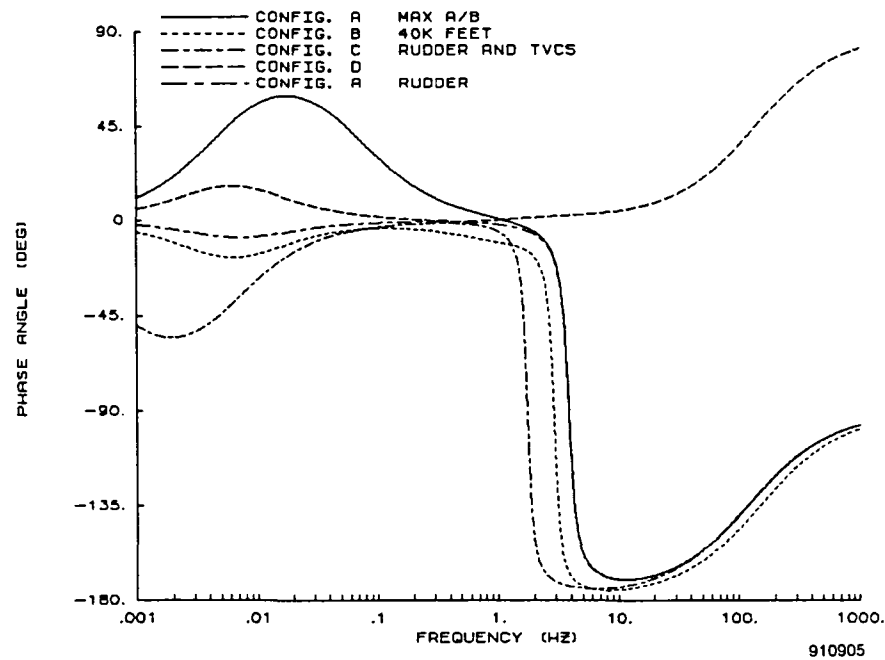

Figure 60. Effects of tail size on sideslip angle phase characteristics at maximum afterburner, 40,000 ft, and M = 0.9 with thrust vectoring.
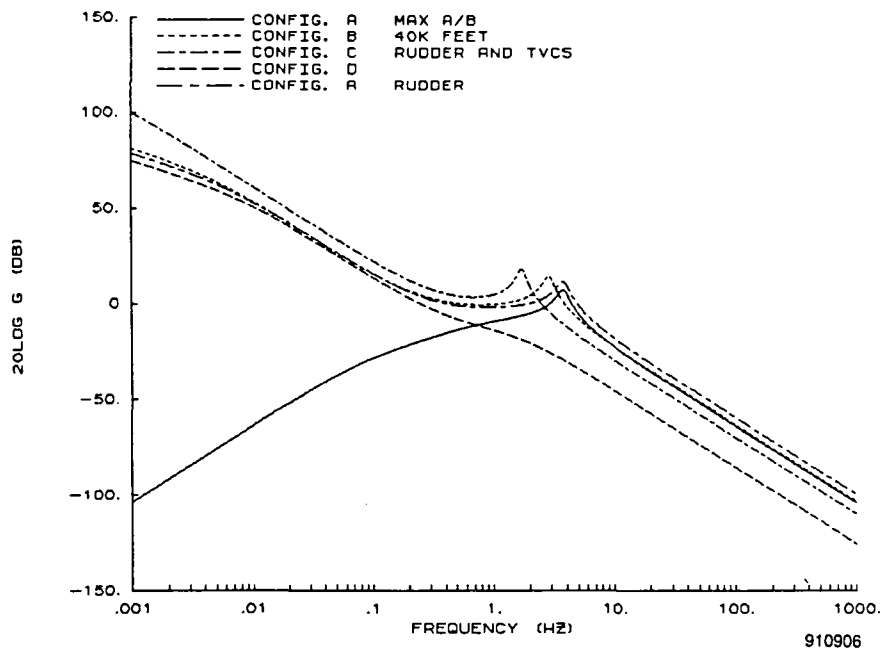
64

Figure 61. Effects of tail size on heading angle magnitude characteristics at maximum afterburner, 40,000 ft, and M = 0.9 with thrust vectoring.
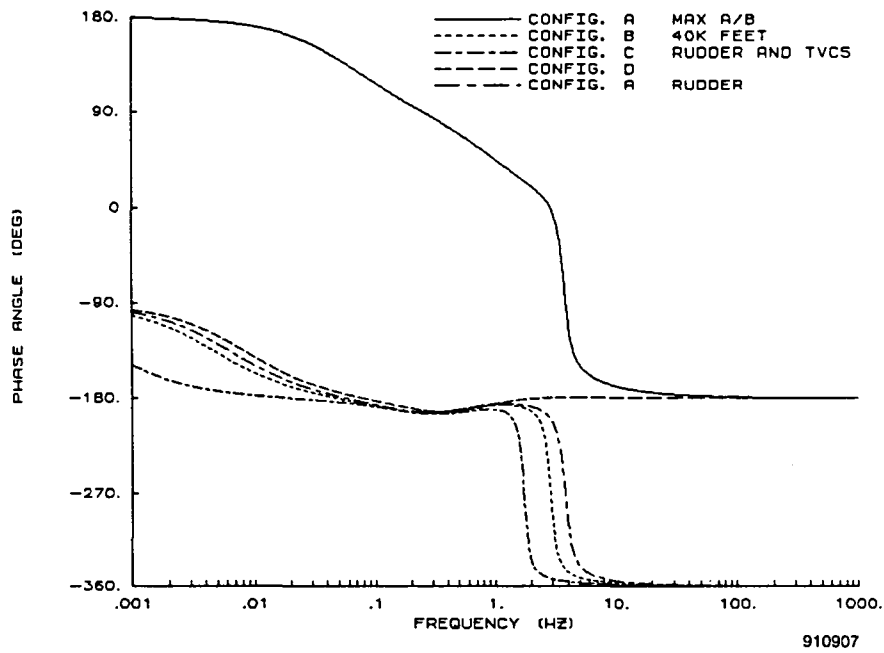

Figure 62. Effects of tail size on heading angle phase characteristics at maximum afterburner, 40,000 ft, and M = 0.9 with thrust vectoring.
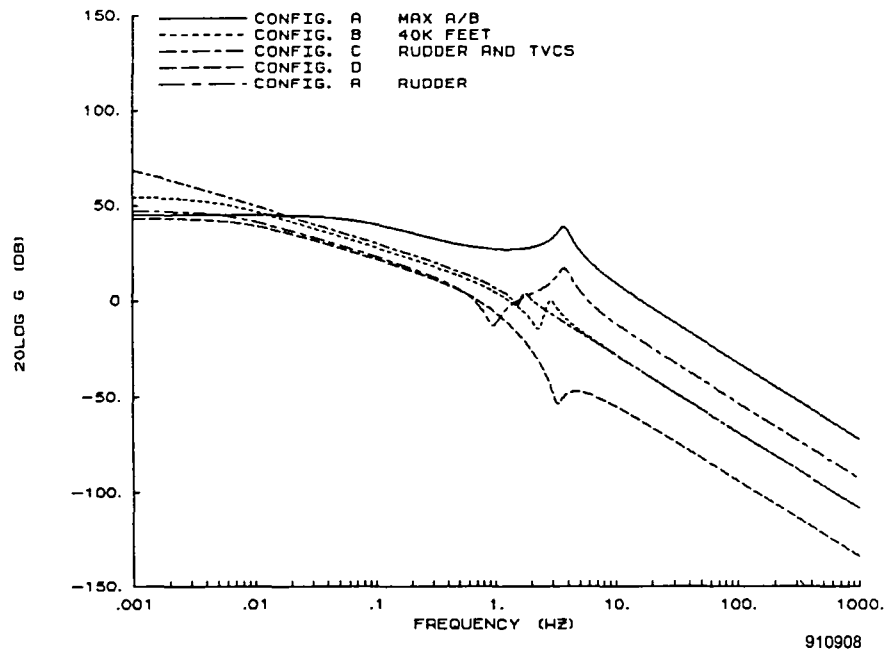
Figure 63. Effects of tail size on bank angle magnitude characteristics at maximum afterburner, 40,000 ft, and M = 0.9 with thrust vectoring.
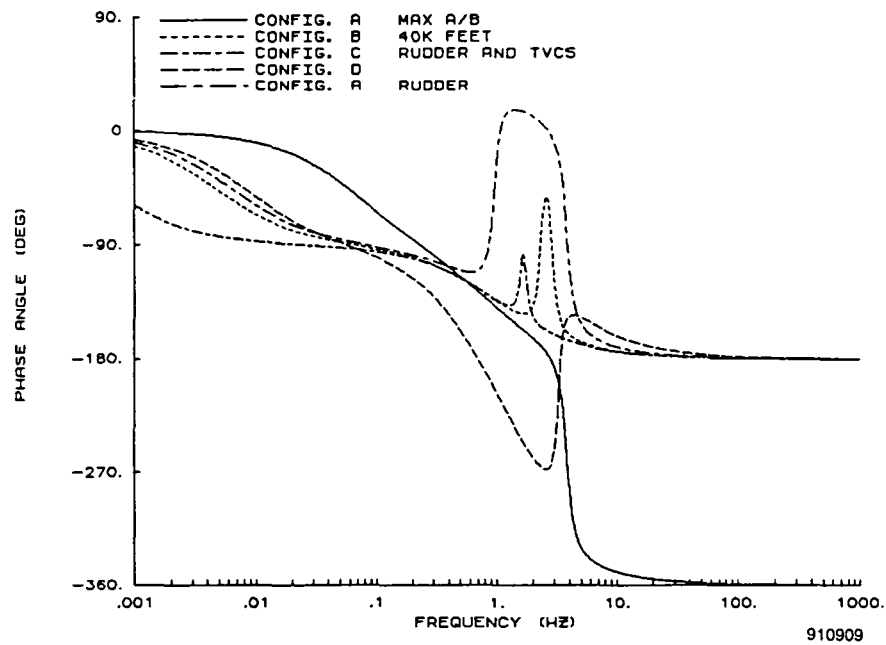

Figure 64. Effects of tail size on bank angle phase characteristics at maximum afterburner, 40,000 ft, and M = 0.9 with thrust vectoring.

66

REPORT DOCUMENTATION PAGE

Public reporting burden for this collection of information is estimated to average 1 hour per response, including the time for reviewing instructions, searching existing data sources, gathering and maintaining the data needed, and completing and reviewing the collection of information. Send comments regarding this burden estimate or any other aspect of this collection of information, including suggestions for reducing this burden, to Washington Headquarters Services, Directorate for Information Operations and Reports, 1215 Jefferson Davis Highway, Suite 1204, Arlington, VA 22202-4302, and to the Office of Management and Budget, Paperwork Reduction Project (0704-0188), Washington, DC 20503.

1. AGENCY USE ONLY (Leave blank)	2. REPORT DATE March 1992	3. REPORT TYPE AND DATES COVERED Corporate Report

4. TITLE AND SUBTITLE

Thrust Vectoring for Lateral-Directional Stability

5. FUNDING NUMBERS

RTOP 533-02-35

6. AUTHOR(S)

Lee R. Peron and Thomas Carpenter

7. PERFORMING ORGANIZATION NAME(S) AND ADDRESS(ES)

NASA Dryden Flight Research Facility
P.O. Box 273
Edwards, California 93523-0273

8. PERFORMING ORGANIZATION REPORT NUMBER

H-1645

9. SPONSORING/MONITORING AGENCY NAME(S) AND ADDRESS(ES)

National Aeronautics and Space Administration
Washington, DC 20546-0001

10. SPONSORING/MONITORING AGENCY REPORT NUMBER

NASA CR-186016

11. SUPPLEMENTARY NOTES

12a. DISTRIBUTION/AVAILABILITY STATEMENT

Unclassified — Unlimited
Subject Category 08

12b. DISTRIBUTION CODE

13. ABSTRACT (Maximum 200 words)

This investigation was conducted to determine the advantages and disadvantages of using thrust vectoring for lateral-directional control and the effects of reducing the tail size of a single-engine aircraft. The aerodynamic characteristics of the F-16 aircraft were generated by using the Aerodynamic Preliminary Analysis System II panel code. The resulting lateral-directional linear perturbation analysis of a modified F-16 aircraft with various tail sizes and yaw vectoring was performed at several speeds and altitudes to determine the stability and control trends for the aircraft compared to these trends for a baseline aircraft. A study of the paddle-type turning vane thrust vectoring control system as used on the National Aeronautics and Space Administration F/A-18 High Alpha Research Vehicle is also presented.

14. SUBJECT TERMS

F/A-18 high alpha research vehicle; High angle of attack; Postexit vanes; Thrust vectoring

15. NUMBER OF PAGES
72

16. PRICE CODE
A04

17. SECURITY CLASSIFICATION OF REPORT	18. SECURITY CLASSIFICATION OF THIS PAGE	19. SECURITY CLASSIFICATION OF ABSTRACT	20. LIMITATION OF ABSTRACT
Unclassified	Unclassified	Unclassified	Unlimited

End of Document